UNIVERSITY OF TOKYO

Digitalized Optical Ring Resonator Gyroscope Using Photonic Bandgap Fiber

by

Xijing WANG

Supervisor

Prof. Kazuo HOTATE, Assoc. Prof. Zuyuan HE

A thesis submitted in partial fulfillment for the
degree of Master of Engineering

in the
DEPARTMENT OF ELECTRONIC ENGINEERING, GRADUATE SCHOOL OF ENGINEERING

August 2008

Acknowledgements

The research presented in this thesis has been carried out at the Department of Electronic Engineering, the University of Tokyo. Working on this project is more than just learning the scientific facts and obtaining the conclusions presented. Rather, it is a training process that helps me to build my scientific and analytical thinking skills.

I acknowledge my debt to those who have helped me along the way. In particular, I wish to express my gratitude to my supervisors, Professor Kazuo Hotate and Assoc. Prof. Zuyuan He for their continued encouragement and invaluable suggestions during the research.

Furthermore I am deeply indebted to all the people at *Hotate, Yamashita and He Lab.* I would like to thank Masuhara-san, Machida-san for solving my daily life problems; Zou-san, Mizuno-san for sharing their experiences in experiment and numerical simulation; Fan-san for studying together ever since the Master's program starts. Support from many others at this lab is also recognized and greatly appreciated. It is, however, not possible to list all here.

I would also like to thank Mr. Satoki Kawanishi from NTT Basic Research Laboratories, although heavily busy, prepares me with intricate PBF samples.

Finally I want to thank my family. The encouragement and support from Dad and Mom, even in my lowest period of study, once again strengthens my belief to keep on moving. My beloved Zhaoxian, always positive and considerate, is a powerful source of inspiration and energy.

Contents

List of Figures

List of Tables

Abbreviations

B-FOG	**B**rillouin **F**iber **O**ptic **G**yroscope
CCW	**C**ounter **C**lock **W**ise
CW	**C**lock **W**ise
ESOP	**E**igen **S**tate **O**f **P**olarization
FOG	**F**iber **O**ptic **G**roscope
FOS	**F**iber **O**ptic **S**ensor
I-FOG	**I**nterferometer **F**iber **O**ptic **G**yroscope
PBF	**P**hotonic **B**andgap **F**iber
PMF	**P**olarization **M**aintaining **F**iber
R-FOG	**R**esonator **F**iber **O**ptic **G**yroscope
SMF	**S**ingle **M**ode **F**iber

To

Dad and Mom

&

my beloved Zhaoxian

for support and encouragement.

Chapter 1

Introduction

This chapter introduces the research background as well as the configuration of the thesis. In the former section, the application, classification as well as working principle of the Fiber Optic Gyroscope (FOG) are introduced. In the latter part, the configuration of the dissertation is presented.

1.1 Research Background

Along with the telecommunication revolution decades ago does the emerge of the fiber optic sensors (FOSs) in the fields of telecommunication, medicine, defense, aerospace, and etc. As one of the FOSs, the FOG has become the most sophisticated type [1, 2]. The FOG is used to detect the rotation with respect to an inertial frame. The working principle is based on the so called *Saganc Effect* as shown in Fig. 1.1. Two lightwaves, propagating in opposite directions in the same closed optical path, show a traveling time difference, which, as expected by the relativistic theory, is proportional to the rotation rate.

Compared with traditional spinning mass gyros, fiber-optic gyros show significant advantages, particularly in short warm-up time, lightweight, maintenance-free, reliable operation, wide dynamic range, low power consumption, and low cost. As a result, the FOGs have been used in a variety of fields, for example in aircraft navigation, oil drilling, rocket controlling, ship navigation, and etc. Figure 1.2 shows the applications of gyros and their required sensitivity.

Basically speaking, there are three kinds of FOGs: interferometer FOG (I-FOG), resonator FOG (R-FOG), Brillouin FOG (B-FOG)as shown in Fig. 1.3. For *all* these

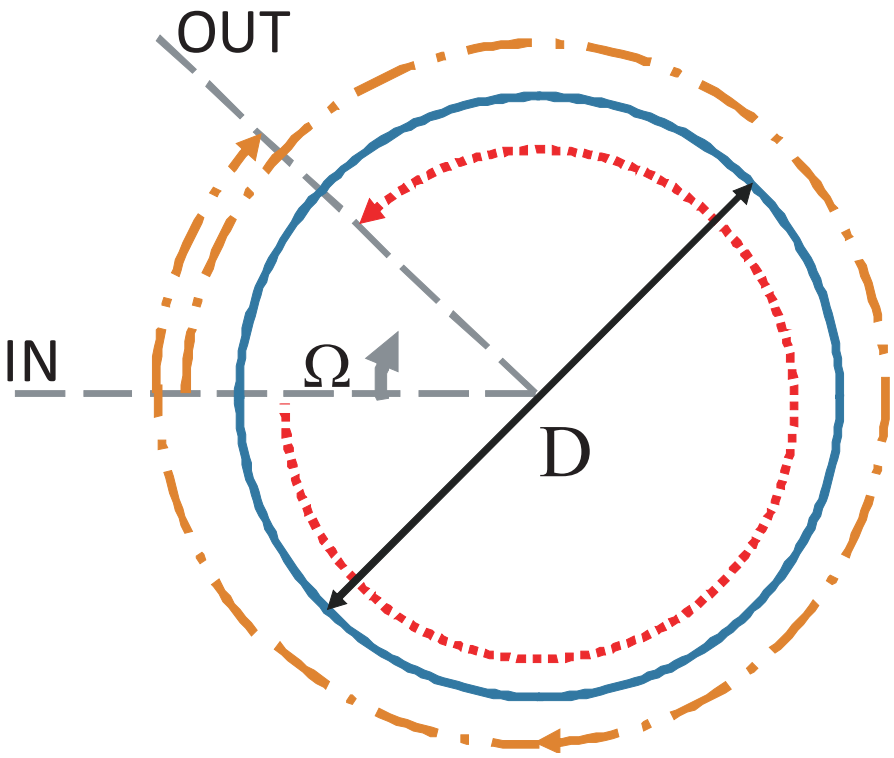

FIG. 1.1: Principle of the *Sagnac* effect.

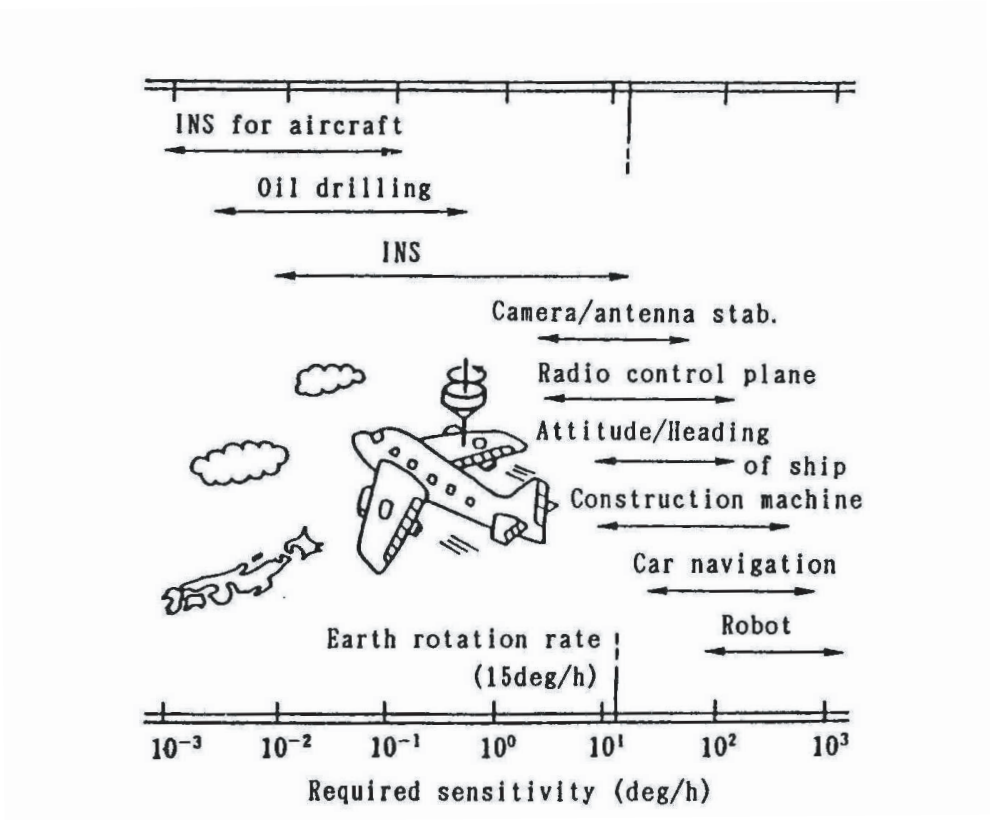

FIG. 1.2: Applications of gyros and their required sensitivity [1].

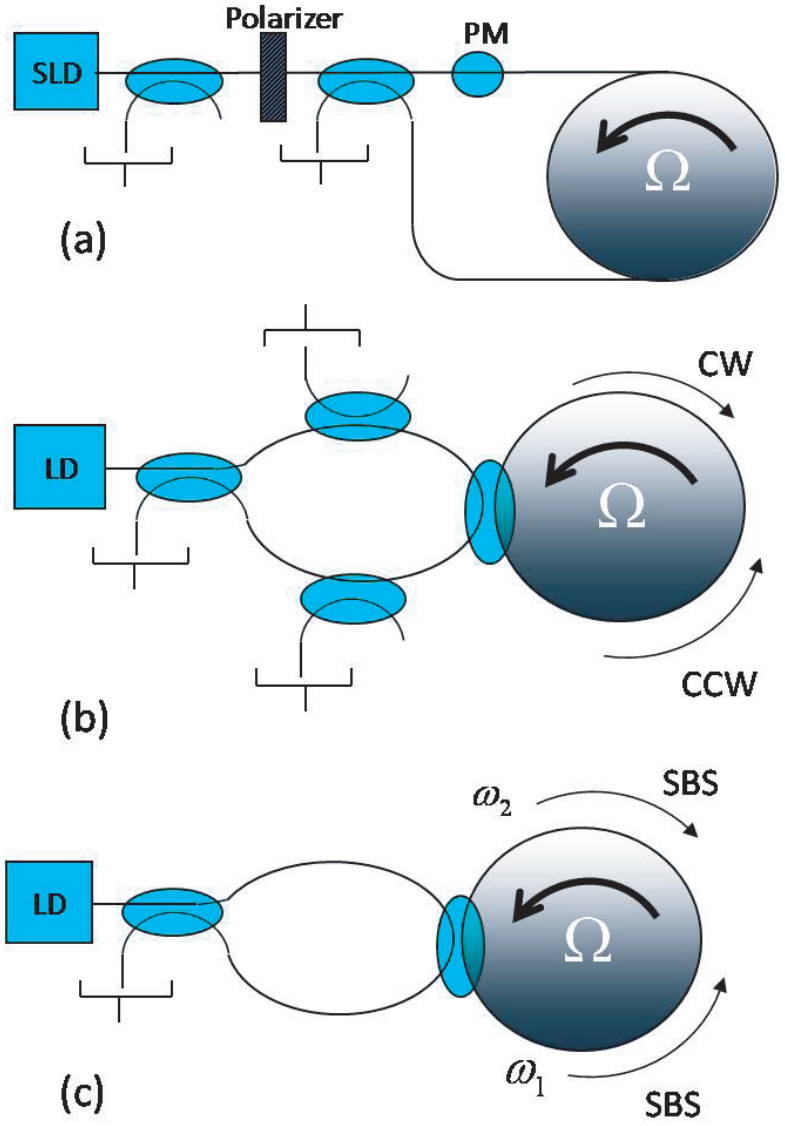

FIG. 1.3: Three basic types of FOG, (a)I-FOG, (b)R-FOG, (c)B-FOG.

types, the rotation speed is related to the phase difference by the equation of:

$$\Delta\Phi = \frac{4kS}{c}\Omega \tag{1.1}$$

where k is the wavenumber, S the area, c the light velocity, Ω the rotation speed, and $\Delta\Phi$ the phase difference, respectively.

In fields of FOGs, all noise factors should be clarified. For example, to achieve the $10^{-7} rad/s$ sensitivity requirement of aircraft navigation, phase difference as small as $1\mu rad$ should be detected. During the past 20 years, many smart engineering methods have been proposed and realized, which makes it possible to instal the I-FOG on the modern Boeing 777 aircraft.

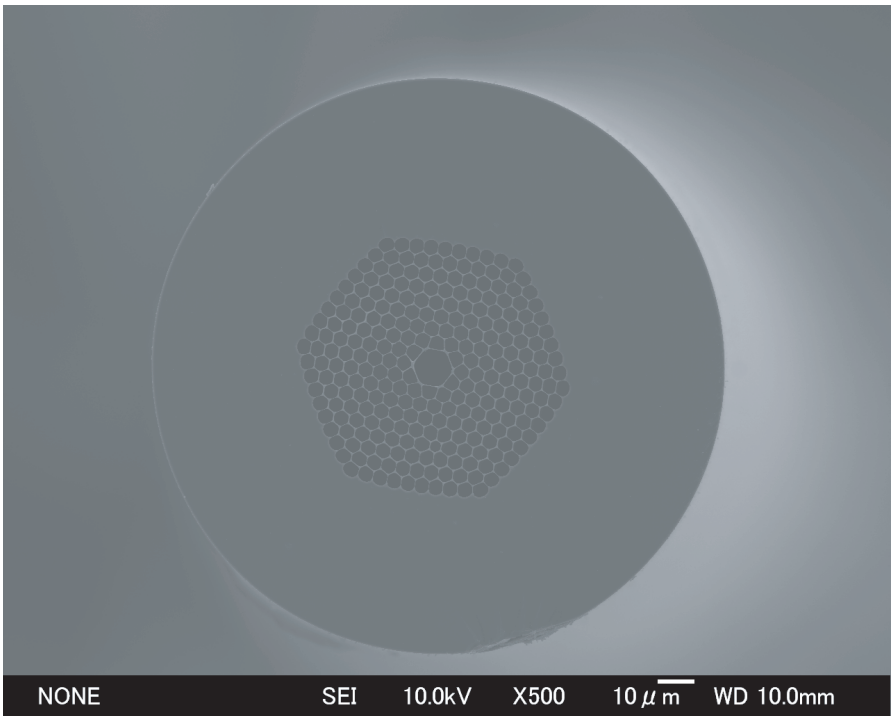

FIG. 1.4: Electron Scanning Micrograph (SEM) of a 7-cell PBF sample from NTT.

This dissertation will focus on one type of the FOGs, the R-FOG. The R-FOG works as a multi-pass ring resonator, with sharp peak/dip at the resonant frequency. By detecting the intensity at the slope of resonance, high sensitivity could be obtained. Besides, a sensing coil of merely 5 to 10 meters is enough to meet the requirement of aircraft navigation, which is much shorter than that of I-FOG. However, there are still some deleterious effects that lead to the bias drift, which needs to be carefully treated.

The Photonic Bandgap Fiber (PBF), as shown in Fig. 1.4, is regarded as one possible solution to reduce the unavoidable noise factors in traditional polarization maintaining fiber (PMF) due to its air-hole structure. Details about this topic would be included in latter sections.

1.2 Configuration of the thesis

The purpose of this thesis is to study noise reduction mechanisms in R-FOG for low speed rotation detection. Throughout it, three aspects are highlighted:

- The adoption of PBF as the sensing coil
- Digital controller design in substitution of analogue circuits

- Numerical analysis of a mathematical model that takes the crosstalk in the coupler into consideration in treating the polarization problem

In Chapter 2, the principle of the R-FOG is reviewed first. Then the noise factors that limit the R-FOG performance are categorized. The traditional engineering solutions are also provided.

In Chapter 3, the topic is extended to the PBF. As we have realized that it is quite difficult to further increase the sensitivity of the system using the traditional sensing coil, some "physical" revolution is necessary. One possible solution is the PBF, which has air holes in its core part. So in this chapter, we talk about the basics of PBF and its advantages in R-FOG system. Besides, resonator characteristics experiment using PBF is demonstrated with its temperature sensitivity measured.

In Chapter 4, quasi-rotation detection using a digital controller developed by ourselves is presented. First, the hybrid digital serrodyne modulation model is built. Related parameters are optimized after numerical calculation. Second, compensation of the imperfect phase modulator 2π voltage is demonstrated with digital feedback loop on. Third, quasi-rotation result is shown with a sensitivity of $0.8^o/s$.

In Chapter 5, the polarization problem is analyzed based on a twice 90^o rotation splicing scheme. In analyzing the scheme, a novel mathematical model that incorporates the crosstalk of the coupler is investigated. Numerical results show that the crosstalk is one of the deleterious factors in limiting the R-FOG performance that should not be ignored. Besides, the possibility to achieve the aircraft navigation requirement using this scheme is verified under certain circumstances.

In Chapter 6, conclusions are drawn based on the results up to now. Finally, future work is outlined.

Chapter 2

Principle of R-FOG and the Noise Factors

This chapter introduces the principle of R-FOG and categorizes the noise factors that limit the system performance. Besides, smart engineering solutions are provided accordingly. Finally, the necessity to introduce the PBF as the sensing coil is also covered.

2.1 Principle of R-FOG

The resonator fiber-optic gyroscope uses a recirculating ring resonator cavity, which is very similar to that of a Fabry-Perot cavity. Around the resonant frequency, output intensity changes greatly according to the phase delay per one turn. Thus, the rotation-induced *Sagnac* effect is largely increased.

As a matter of fact, there are two resonators, one corresponding to the clockwise (CW) path and the other one corresponding to the counter clockwise (CCW) path. When the R-FOG rotates, these two resonant frequencies differ from each other by:

$$\Delta f = \frac{D}{n\lambda}\Omega \tag{2.1}$$

where Δf is the resonant frequency difference, D the diameter of sensing coil, n the refractive index of the light path, λ the wave length. This is depicted in Fig. 2.1.

Up to now, we have only talked about the resonator and its CW and CCW resonant characteristics. *How can they serve to detect the rotation action?* This is facilitated by the sophisticated modulation and demodulation techniques that transform the lightwave

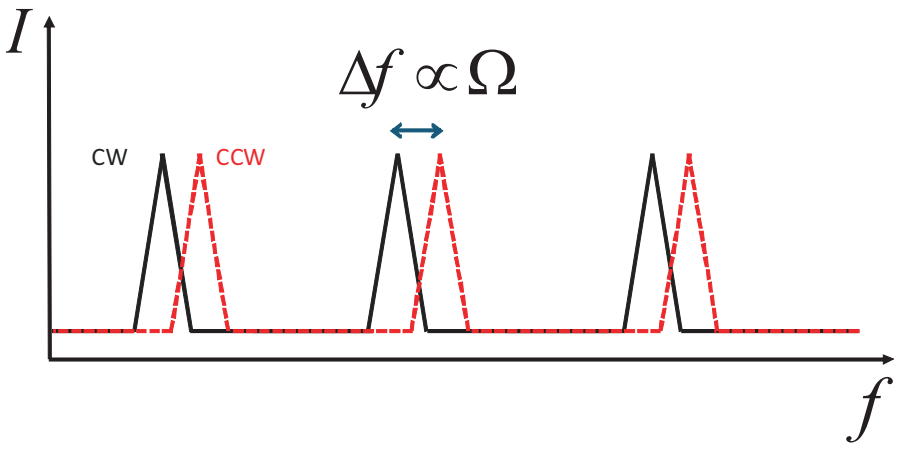

FIG. 2.1: Shifted resonant peaks when R-FOG rotates.

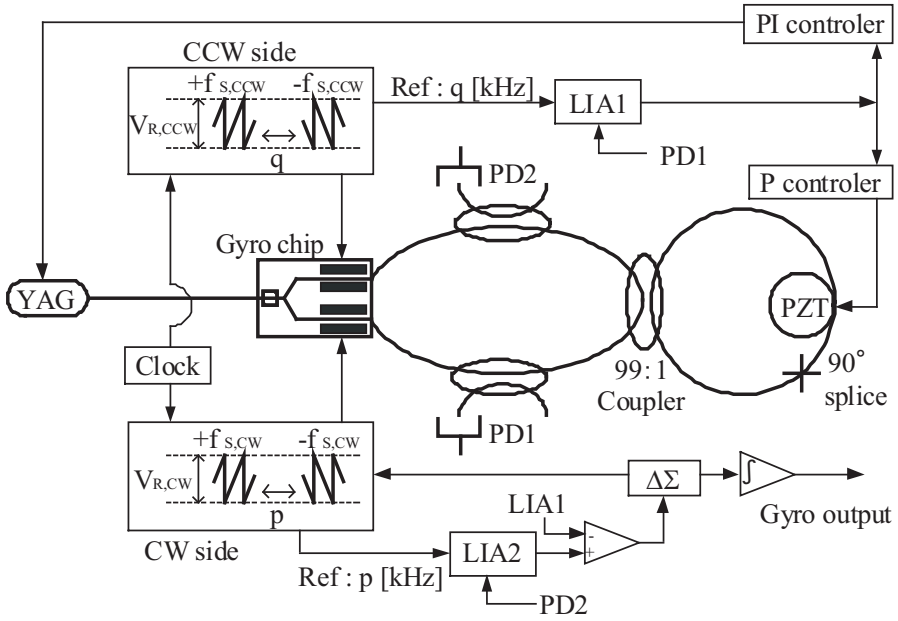

FIG. 2.2: A typical R-FOG experiment system setup [3].

phase information into the electrical information that is detected and measured as a voltage signal.

Figure 2.2 is a typical experiment setup of the R-FOG system using the so called Digital Serrodyne modulation [4]. The open loop mode operates in a manner that first locks the resonant frequency of the CCW side to the central frequency of the laser diode; then subtracts the output of CW side from the CCW side to read the frequency difference out. The closed loop mode adds an additional step that lock the resonant frequency of CW side to the central frequency of laser diode. The feedback error signal is also the final output that corresponds to the input rotation. The answer to the question why

two resonators ,i.e. CW and CCW are needed simultaneously to measure the rotation is that the thermal noises are canceled out by the subtraction operation.

2.2 Noise Factors and Traditional Solutions

To detect rotation as slow as that of earth rotation, stringent requirement is put on the stability of the R-FOG system, which means all noise factors should be clarified and treated.

2.2.1 Rayleigh Backscattering

According to [5], the electric field output of one side is actually the sum of the signal wave and the backscattered wave due to the Rayleigh Backscattering within the fiber. Assume the detected electric field is $E(t) = E_S(t) + E_{SD}(t)$, the intensity is:

$$\overline{E(t)E^*(t)} = \overline{|E_S(t)|}^2 + 2Re[\overline{E_S(t)E^*_{SD}(t)}] + \overline{|E_{SD}(t)|}^2 \tag{2.2}$$

where $E_S(t)$ is the signal wave, and $E_{SD}(t)$ is backscattered wave. From this equation, it can be realized that not only the backscattered wave itself, but also their interference results in large drift in the output.

To get rid of the backscattered term (the third term) in Eq. 2.2, a typical anti-measurement is to apply different frequency modulation or phase modulation to the CW and CCW lightwaves before they enter the ring. The modulation shifts the waves to separate frequency and make the backscattered wave go out of the detection band.

To separate the first term from the second term, one method is to suppress the carrier of the input waveform by proper frequency modulation as in [6]. Another method is to generate special modulation waveforms that makes difference in the optical frequency between the CW and the CCW waves as in [3].

2.2.2 Polarization Drift

It is well known that a PMF actually guides two polarization modes with slightly different velocities due to the birefringence. This means that the PMF supports two sets of resonance corresponding to two polarizations modes, which are usually referred to as the two Eigen State Of Polarizations (ESOPs) [7].

The two resonant peaks drift across each other easily if the local temperature is slightly changed. This is because the PMF belongs to the stress induced birefringent type, which is very sensitive to the temperature. It degrades the RFOG performance greatly. Several solutions have been proposed up to now. As one example, two polarizers are included at the input ports in [8]. Yet the extinction ratio should be high enough. Another solution is to splice two PM fibers together with a 90^o polarization rotation at the splicing point [9]. By splicing, the two resonant peaks are set π phase away from each other. Thus, the influence between each other is reduced by a large amount. However, this is still not ideal considering that two ESOPs are simultaneously excited.

Another possible solution would be the reduction of temperature sensitivity of the fiber. In other words, the two exited ESOPs remain relatively stable in a changing temperature environment. This can be realized by including PBF as the sensing coil which will be talked about in later chapters.

2.2.3 Kerr Effect

The Kerr Effect is observable when the CW and CCW lightwaves are of different intensities. The local birefringence felt by the electronic field heading for one direction is determined by both itself and the one moving toward the other direction. The "other" wave even poses a determination factor twice stronger.

Several solutions regarding the Kerr effect have been reported. In [10], intensity of one of the two waves is directly changed; in [11], the resonant frequency of either one of the lightwaves is changed using the digital serrodyne phase modulation. This can be explained as that in a closed loop operation, the CW and CCW wave intensities are balanced only if the frequency component of the modulating square waveform is zero.

2.2.4 Shupe Effect

The Shupe Effect [12] is another cause of bias drift. It is resulted from by the uneven distributions of thermal fluctuations in the sensing loop with respect to the loop's mid point, which gives rise to the different phase delay between the CW wave and the CCW wave. The traditional solution is to apply some sophisticated coiling method.

2.3 Conclusion

In this chapter, we first reviewed the working principle of a R-FOG system, which takes advantages of the sharp dip/peak around the resonant frequency. Then we listed the noise factors in R-FOG and their traditional engineering solutions. Although these methods can work for some degree, it is quite hard to increase the R-FOG sensitivity any more. This calls for the modifications in the body of the sensing coil, which will be discussed in detail in the next chapter.

Chapter 3

PBF Ring Resonator

After reviewing the properties of PBF, we demonstrate the resonant characteristic experiment using PBF. Besides, the PBF temperature sensitivity is measured based on the constructed ring resonator.

3.1 Photonic Bandgap Fiber Basics

Photonic bandgap fibers guide light by confining it within a periodic array of microscopic air holes that run along the entire fiber length [13, 14]. Its fabrication process is shown in Fig. 3.1. A stack of glass tubes and rods is first constructed. Then a part of them at the central area is taken out to create the macroscopic "preform" according to the required photonic crystal structure. It is then fused together and drawn down to fiber using a standard fiber drawing tower.

Simply speaking, the PBF can guide light because the micro structures inside the PBF constitute "bandgaps" that prohibit the propagation of electrical fields in any direction due to the multi Bragg reflection. The most simple example would be the one-dimensional fiber Bragg grating or the multi-layer stacked photonic crystal as shown in Fig. 3.2. This structure is able to transmit electromagnetic waves at certain frequencies while reflecting the others. Therefore, the wave guiding theory is totally different from that of the traditional solid-core fiber, which confines the light inside the core due to the index contrast [15]. This also promises the unique properties of PBF that are positive from the view of fiber gyroscope.

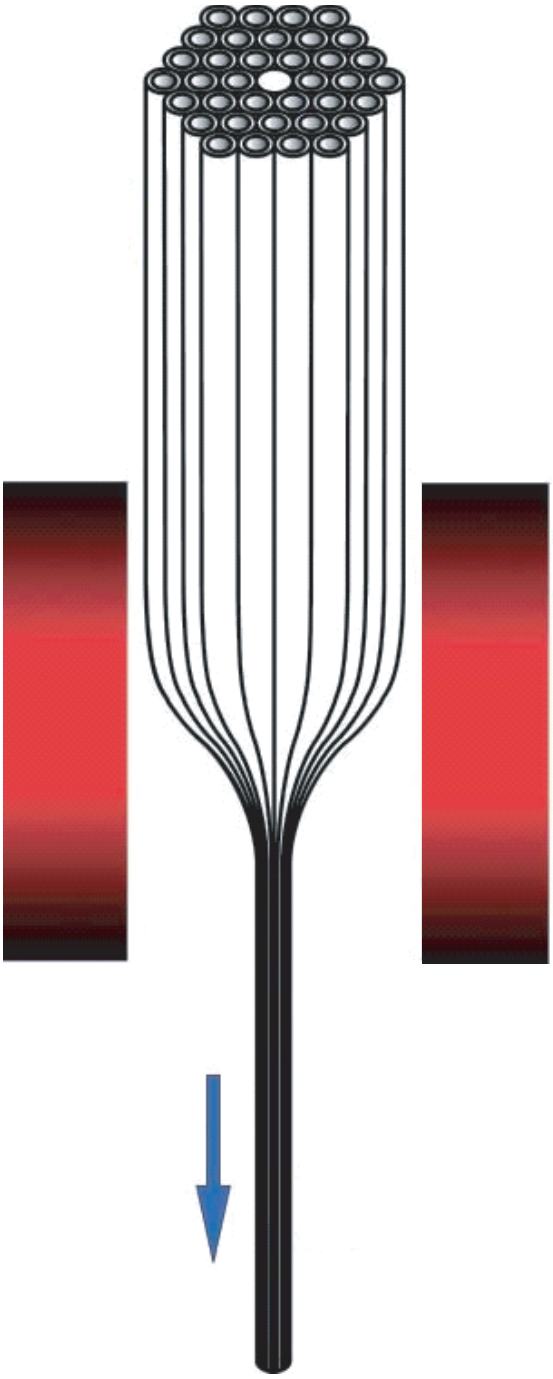

FIG. 3.1: Photonic Bandgap Fiber fabrication process [14].

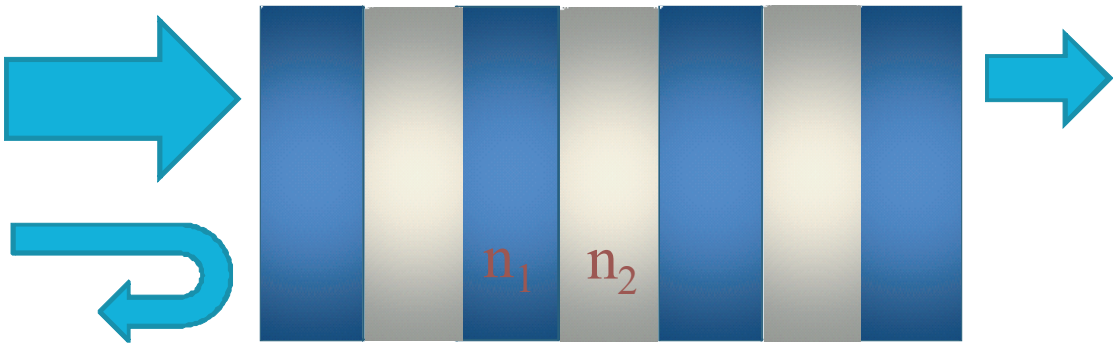

FIG. 3.2: Bandgap effect in one-dimensional photonic crystal.

3.2 Photonic Bandgap Fiber Properties

Unlike the traditional fibers, which guide the lightwave in the silica, PBF guides light almost in its air core. And it has shown remarkable new properties that can outperform conventional fibre in several respects.

3.2.1 Reflection Coefficient

The reflection coefficient represents the fraction of the incident light that is reflected into the backward direction. This degrades the system performance a lot in fiber sensors, communication systems, lasers, and etc.

The reflection coefficient for PBF is expected to be relatively low. This is because the light in PBF propagates through air, while, in PMF, light interacts with the silica all the time. If the scattering coefficient is α, then:

$$\alpha_{PBF} = \eta \alpha_{silica} \tag{3.1}$$

According to [16], η is to the order of 10^{-2}.

A problem that should be noted is that while the reflection of PBF terminated in air is found to be low, much stronger reflection is expected for a solid termination as in the case of splicing a PBF to a SM fiber. This is because the large refractive index difference at the boundary. In other words, in designing the R-FOG, a free space configuration would be better in reducing the backscattered noise. This also means that the development of PBF based optical passive components should be put in the schedule.

3.2.2 Temperature Sensitivity

The temperature sensitivity property is related to the polarization drift induced noise in R-FOG. It influences the phase difference between the excited two ESOPs. The temperature sensitivity is defined as:

$$\frac{\partial B}{\partial T} = \frac{\Delta\phi}{\frac{2\pi}{\lambda} L \Delta T} \tag{3.2}$$

where B is the modal birefringence that defines the effective refractive index difference between orthogonal linear polarization modes, $\Delta\phi$ the temperature induced phase shift between the two polarization modes, and L the fiber length that is exposed to the temperature change of ΔT. For a traditional PMF, this parameter is to the order of $10^{-5}/^{o}C$, which is relatively high due to the stress induced birefringence.

In [17], the author compares the temperature sensitivity of PBF with that of SMF, and found that it was 5 times lower.

3.2.3 Kerr Effect Coefficient

The Kerr effect coefficient of conventional single mode fiber is $2.5 \times 10^{-16} cm^2/W$, which is about three orders of magnitude larger than that of air, i.e. $2.9 \times 10^{-19} cm^2/W$. The effective Kerr nonlinearity in a particular air-core fiber is reported to be $3.02 \times 10^{-19} cm^2/W$ [18].

3.2.4 Shupe Effect Coefficient

This is reduced by 3.6 times in a PBF compared with that of a traditional SMF [16]. This is because in the PBF, most of the energy travels in the air, and the index of air is much weakly dependant on temperature. This effect would be further reduced by carefully design of the thickness of the fiber jacket and the material.

3.3 PBF Ring Resonator Experiment

Experiments are carried out to demonstrate: (1) the PBF ring resonator characteristics; (2) the temperature sensitivity of PBF.

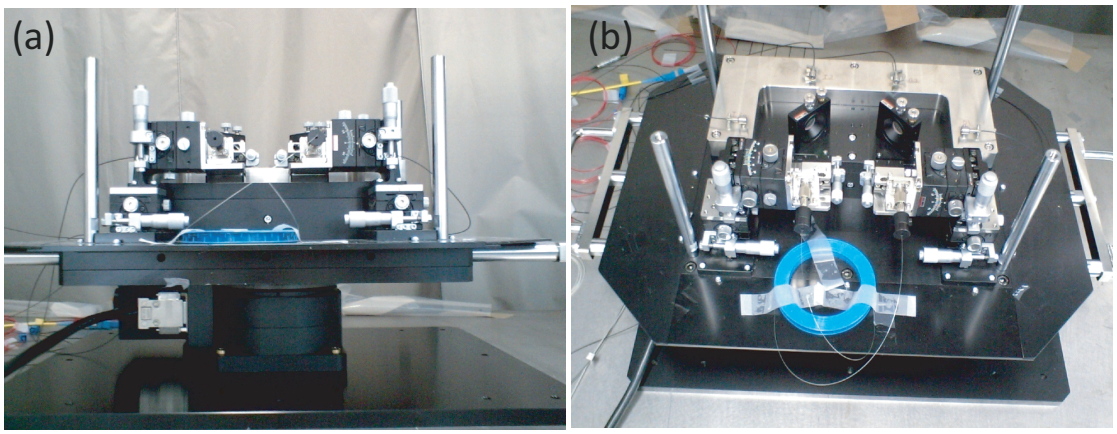

FIG. 3.3: Free space optical alignment system: (a) front, (b) above.

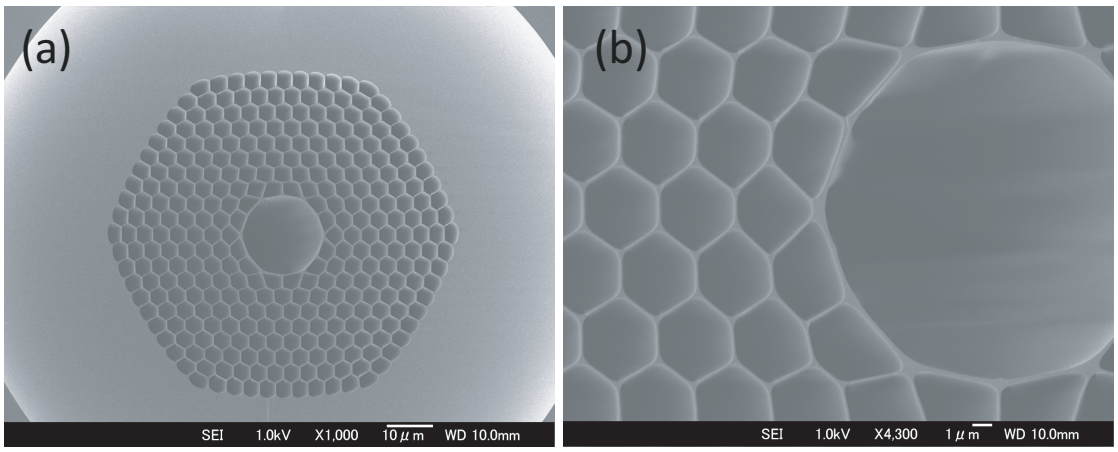

FIG. 3.4: Electron Scanning Micrograph (SEM) of a 19-cell PBF sample from NTT: (a) ×1000, (b) ×4300.

3.3.1 Ring Resonator Characteristics

Free space optical components are adopted to couple light into the fiber as depicted in Fig. 3.3. The beamsplitter has a high reflectivity as up to 99% and serves as the "coupler" to recirculate most of the energy inside the ring. To realize the fine alignment, the fiber is mounted on a three dimensional stage with 6 degrees of freedom. There are some advantages to use the bulk optics: (1) low backscattering at the fiber to free space interface, since both of their refractive index are unit; (2) low polarization crosstalk of the beamsplitter, while that of the coupler is considered to be one of the major sources of crosstalk in the traditional R-FOG.

The PBF in this experiment has a 19-air-hole structure as shown in Fig. 3.4. The core part has a diameter of $17\mu m$, while the periodic micro structure has a diameter of $3\mu m$.

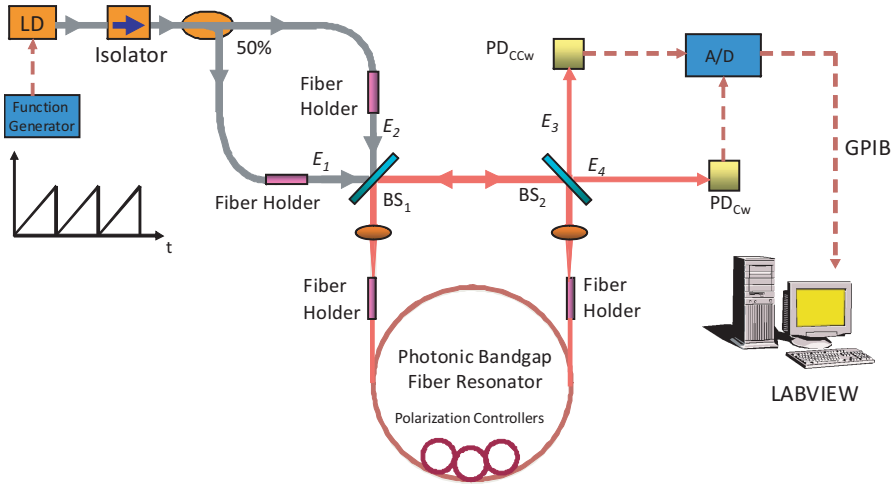

FIG. 3.5: Experiment setup for resonance characteristics measurement.

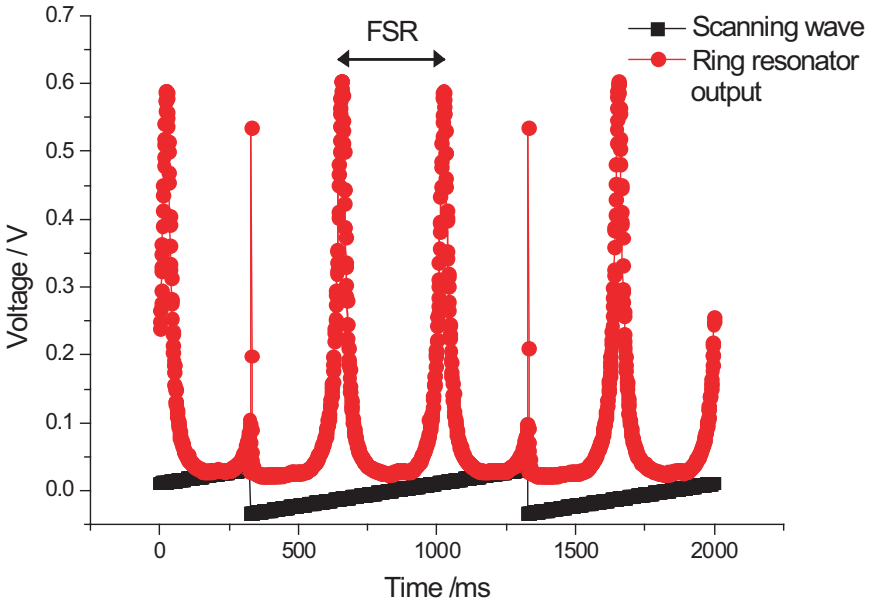

FIG. 3.6: PBF ring resonator resonance characteristics.

To observe the resonance characteristics of the PBF ring resonator, the central frequency of the lightwave from the DFB laser diode with a bandwidth of $70kHz$ is scanned by a sawtooth waveform as depicted in Fig. 3.5. The result is shown in Fig. 3.6, with free spectral range (FSR) and Finesse being 117MHz and 20, respectively.

3.3.2 PBF Temperature Sensitivity

According to the Eq. 3.2, the temperature coefficient describes temperature induced phase shift between the two polarization modes. In a ring resonator, this can be deduced

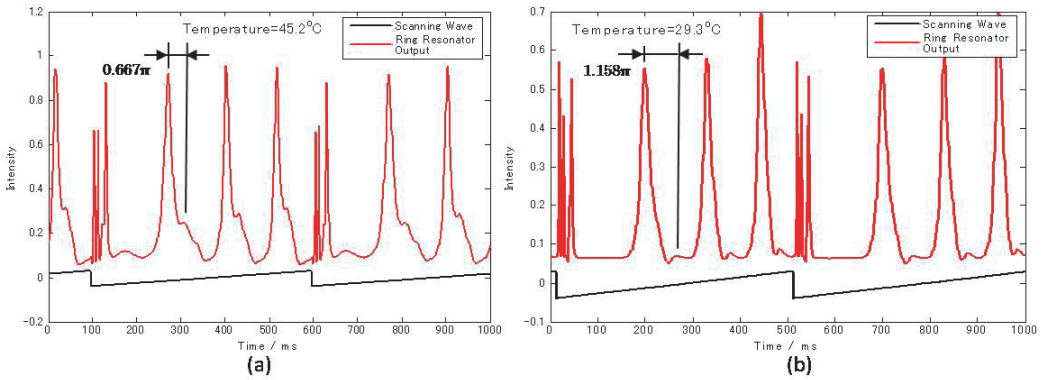

FIG. 3.7: Phase difference between 2 ESOPs (a) 45.2^oC, (b) 29.3^oC.

by recording the phase difference between two neighboring peaks that are representative of the two eigen state of polarizations (ESOPs) as the temperature changes.

Before the experiment, we excite two ESOPs intentionally. Besides, we stick the same fiber to a temperature controller and increase the temperature step by step manually. Figure 3.7(a) shows the case of 0.667π phase difference when the temperature is 45.2^oC; Fig. 3.7(b) depicts the case of 1.158π phase difference when the temperature is 29.3^oC. This indicates the temperature coefficient to be 3.74×10^{-8}, which is 100 times lower than that of PMF. In other words, more stable polarization performance of the RFOG could be expected by using the PBF as the excited two peaks are less sensitive to the temperature variations.

3.4 Conclusion

In this chapter, we first reviewed the reported reflection coefficient, the temperature sensitivity, the Kerr effect coefficient, and the Shupe effect coefficient of PBF. These results show a promising future of R-FOG based on PBF. Later, experiments are carried out to test the resonant characteristics of the PBF based ring resonator. We found that the PBF is much stable to temperature disturbances.

Chapter 4

Digital Controller Design and Quasi-rotation Test

This chapter focuses on the digital serrodyne modulation scheme and the related digital circuit. We first introduces the concept of rotation detection by digital serrodyne modulation. Then, we optimize some parameters by mathematical modeling. Next, we discuss the effect of 2π voltage of the phase modulator. Finally, we experimentally verifies the ideas of rotation measurement and 2π voltage compensation based on the digital controller.

4.1 Principle of Digital Serrodyne Modulation

4.1.1 Frequency Shift Effect

The so called serrodyne modulation is a scheme that modulates the phase of incident lightwave with a sawtooth waveform whose amplitude is 2π as shown in Fig. 4.1(a). In the ideal case, it shifts the lightwave frequency by an amount of $\Delta\omega$. Compared with the frequency modulation schemes, it avoids additional intensity modulation. However, it is quite difficult for the analogue serrodyne modulation to keep constant modulation amplitude and slope. Therefore, a digitalized version as shown in Fig. 4.1(b) was proposed in [4]. And it has also been approved that the digitalized version is equivalent to the analogue waveform so long if the step duration of τ equals to the one turn transmission time.

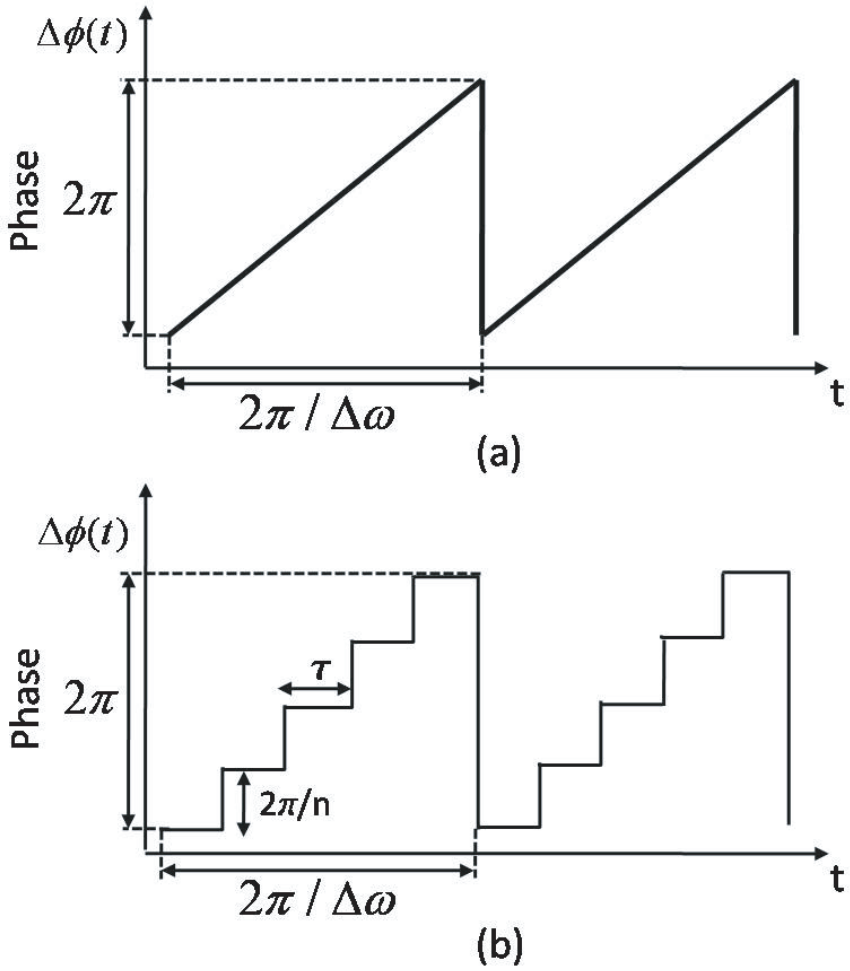

FIG. 4.1: Serrodyne modulation waveform: (a) analogue (b) digitalized.

4.1.2 Rotation Detection

Next, we will explain the principle of resonant point detection using a hybrid digital serrodyne modulation whose shifted frequency is $+\Delta f$ in the first half of period and $-\Delta f$ in the second half, with each period lasting for a duration of $1/f_{rp}$ as shown in Fig. 4.2(a). Denote the central frequency of input waveform to be f_0. If f_0 equals to the resonant frequency, the output of the photo detector is a DC signal as shown in Fig. 4.2(b). Otherwise, the output would be a square waveform with the frequency of f_{rp} and the amplitude of $I_2 - I_1$ as shown in Fig. 4.2(c). Therefore, by synchronously detecting the f_{rp} component in the photoreceptor output, whether the lightwave frequency is equal to the resonant frequency or not can be determined. By measuring its intensity, it is also possible to tell how far away the lightwave frequency is from the resonant frequency by referring to the demodulation curve.

How can we detect the rotation by the above scheme? Let's refer to the traditional analogue system as depicted in Fig. 2.2. The light propagating in the CCW side is

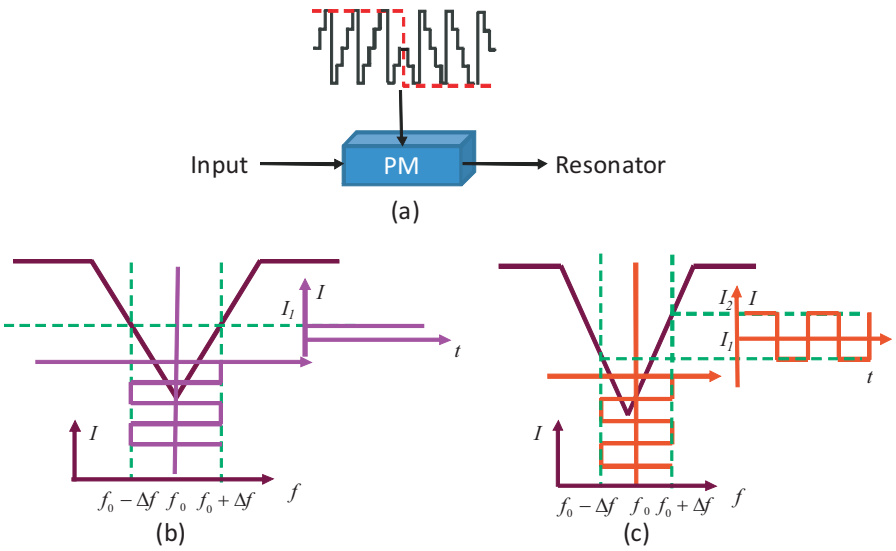

FIG. 4.2: Resonance point detection scheme. PM: phase modulator. (a) Hybrid digital serrodyne modulation; (b) Photodetector output when light frequency is equal to the resonant frequency; (c) Photodetector output when the light frequency is away from the resonant frequency.

modulated by a hybrid digital serrodyne waveform with a shifted frequency of $\pm f_{s,ccw}$ and a repetition frequency of q. When it arrives at the detector PD1, it is demodulated by the lock-in amplifier LIA1 with the frequency of q. The central wave frequency of f_0 is always locked to the resonant frequency by two feedback loops: one to the laser diode itself to track the slow drift and the other one to the PZT to track the fast variation. On the other hand, the CW side is modulated by another hybrid digital serrodyne waveform ($\pm f_{s,ccw} \neq \pm f_{s,cw}$ and $q \neq p$). In open loop operation, the synchronous detection of the output at PD2 is subtracted from that of PD1 to obtain the gyro rotation, since the voltage is linearly related to the resonant frequency difference. In the closed loop operation, the output is fed back to the height of each step to modify the shifted frequency $\pm f_{s,cw}$.

4.1.3 Rayleigh Backscattering Noise Reduction

One advantage of this hybrid digital modulation is that it effectively reduces the backscattering noises by the frequency division multiplexing scheme [4]. Suppose that the light traveling in the CCW direction is the signal and that the light heading for the CW direction is backscattered at some point inside the resonator. In the ideal case that the 2π voltage of the phase modulator is reached, the CCW and CW wave are shifted to different frequencies, i.e. $f_0 \pm \Delta f_{CCW}$ and $f_0 \pm \Delta f_{CW}$. Therefore, by synchronously detecting the output from the photodetector with the repetition frequency of f_{rp}, the third term in Eq. 2.2 in representing of the Rayleigh backscattered intensity will not

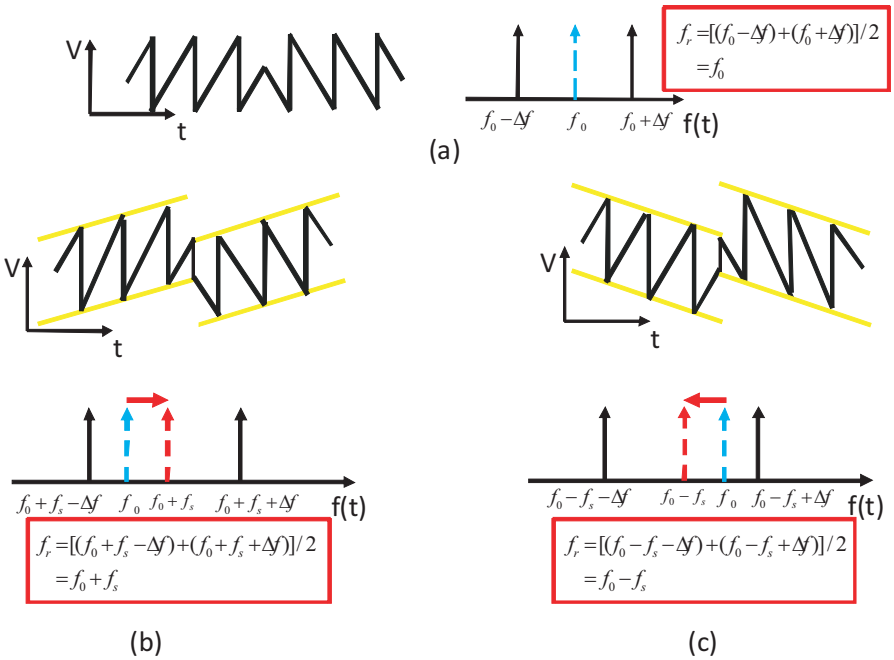

FIG. 4.3: Emulation of rotation by hybrid digital serrodyne modulation. (a) Original hybrid digital serrodyne; (b) central frequency shifted by "$+f_s$"; (c) central frequency shifted by "$-f_s$"

appear. Besides, by appropriately choosing the modulating parameters, the interference term in Eq. 2.2 will go out of the detection band.

4.1.4 Emulation of Rotation Induced Resonant Frequency Shift

In the quasi rotation measurement, if the central frequency of the CCW lightwave is locked to the resonant frequency, an additional central frequency shift in the CW side is needed to emulate the situation that resonant frequencies differ from each other as R-FOG rotates. To clarify this, let's take Fig. 4.3(a) as an example. If f_r, f_0, Δf, f_s stand for the resonant frequency, lightwave central frequency, base serrodyne shifted frequency, and additional frequency shift separately, what the R-FOG takes for as the resonant frequency in one period of hybrid digital serrodyne modulation is the averaged frequency, shifted amount included. Therefore, the gyro thinks that the CW side has a resonant frequency of $f_r = [(f_0 - \Delta f) + (f_0 + \Delta f)]/2 = f_0$. Since it also regards f_0 as the resonant frequency of the CCW side, no rotation has happened. Fig. 4.3(b) shows the case of upshifted central frequency. A linear waveform with positive slope $+f_s$ is added to the base throughout the whole period. The resonant frequency now is $f_r = [(f_0 - \Delta f + f_s) + (f_0 + \Delta f + f_s)]/2 = f_0 + f_s$. It is ahead of the resonant frequency of CCW side by f_s, which might be ascribed to the rotation. The same is true if a negative linear waveform is added to the base waveform to imitate the downshifted central frequency case as shown in Fig. 4.3(c).

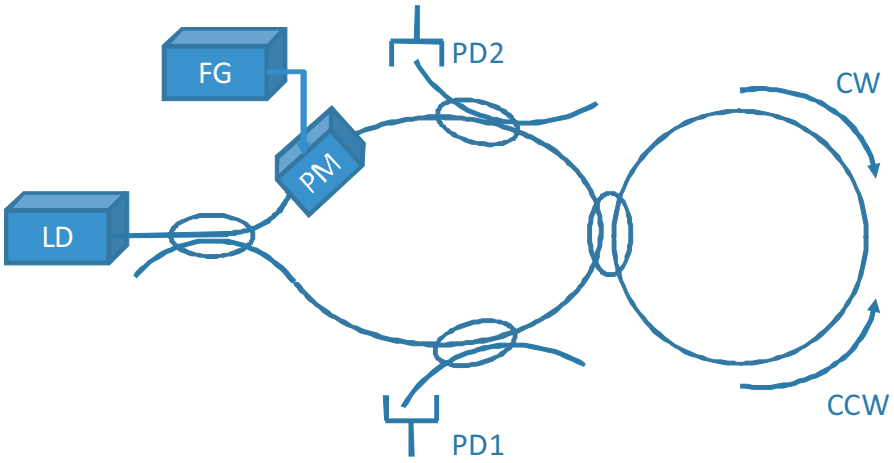

FIG. 4.4: Mathematical model of digital serrodyne modulation. LD: laser diode; PM: phase modulator; PD: photodetector; FG: function generator.

4.1.5 Mathematical Modeling and Parameter Optimizing

For simplicity, the mathematical modeling process is based on the analogue serrodyne modulation scheme, since the digital type has the same effect if the step duration τ equals to that of the one turn transmission time. The target of this model is to optimize the shifted frequency parameter Δf.

Figure 4.4 shows the mathematical model. To detect the resonance point and obtain the feedback error signal, the PM is driven by a hybrid digital serrodyne signal with the shifted frequency of $\pm\Delta f$ and repetition frequency of f_{rp}.

The electronic field at PD1 is:

$$E_1(t) = E_0 e^{j\omega t}(e^{j\Delta\Phi(t)}\beta - \gamma\sum_{n=1}^{\infty}\delta^{n-1}e^{-jn\omega\tau}e^{j\Delta\Phi(t-n\tau)}) \tag{4.1}$$

and,

$$\begin{aligned}\beta &= \lambda_{CT}\sqrt{\kappa_C}\\ \gamma &= \lambda_{CR}^2\kappa_C\lambda_L\\ \delta &= \lambda_L\lambda_{CT}\sqrt{\kappa_C}\end{aligned}$$

where E_0 is the amplitude of the input electronic filed, ω the central frequency, τ the one turn transmission time, κ_C the coupling constant, $1-\lambda_{CT,CR}^2$ the loss of the transmission and the reflection port of the coupler, and $1-\lambda_L^2$ the fiber induced one turn transmission loss (splicing loss included). Therefore, β is the amplitude transmission coefficient of the coupler. And δ is the one turn amplitude transmission coefficient of the ring.

Besides, the serrodyne modulation signal is:

$$\Delta\Phi(t) = \Delta\omega t \tag{4.2}$$

The finesse is defined as:

$$F = \frac{\pi\sqrt{\delta}}{1-\delta} \tag{4.3}$$

The intensity at PD1 with single shifted frequency $\Delta\omega$ is:

$$|E_1(t)|^2 = E_0^2(\beta^2 - \frac{2\beta\gamma(\cos(\omega+\Delta\omega)\tau)}{1-2\delta(\cos(\omega+\Delta\omega)\tau)+\delta^2} + \frac{\gamma^2}{1-2\delta(\cos(\omega+\Delta\omega)\tau)+\delta^2}) \tag{4.4}$$

When the PM is driven by a hybrid serrodyne waveform as stated above, and when the central frequency is not equal to the resonant frequency, there would be a square wave with amplitude of $I_2 - I_1$ and frequency of f_{rp} at PD1. The Fourier transform expansion is:

$$I_{out} = \frac{I_2 - I_1}{2} + 2\frac{I_2 - I_1}{\pi}(\sin f_{rp}t + \frac{\sin 3f_{rp}t}{3} + \frac{\sin 5f_{rp}t}{5} + \cdots) \tag{4.5}$$

Substituting Eq. 4.4 into Eq. 4.5, the f_{rp} component of the I_{out} is:

$$I_{out,f_{rp}} = \frac{2E_0^2}{\pi}(\frac{2\beta\gamma\cos(\omega+\Delta\omega)\tau+\gamma^2}{(1-\delta)^2+4\delta\sin^2\frac{(\omega+\Delta\omega)\tau}{2}} - \frac{2\beta\gamma\cos(\omega-\Delta\omega)\tau+\gamma^2}{(1-\delta)^2+4\delta\sin^2\frac{(\omega-\Delta\omega)\tau}{2}}) \tag{4.6}$$

A numerical calculation has been carried out to show that the hybrid serrodyne modulation scheme has a sharp slope around the resonant frequency as shown in Fig. 4.5.

The derivative of the Eq. 4.4 around the resonant frequency is the sensitivity of the hybrid serrodyne modulation.

$$G(\Delta\omega) = -16E_0^2\beta\gamma(1+2\gamma^2\delta+\delta^2)\tau\frac{\sin\Delta\omega\tau}{((1-\delta)^2+4\delta\sin^2(\Delta\omega/2))^2} \tag{4.7}$$

Figure 4.6 shows the numerical calculation of the demodulation sensitivity as a function of the shifted frequency $\Delta\omega$.

The shot noise determined sensitivity is used as another scale to optimize the modulation parameters. This limit is reached if the rotation induced current $\Delta I_{out,f_{rp}}$ is equal to the shot noise induced current $\Delta i_{out,f_{rp}}$. Suppose that the lightwave central frequency is locked. By linear approximation of the synchronous detection output, the frequency shifted by an amount of ΔF would result in a signal after demodulation:

$$\Delta I_{out,f_{rp}} = G(\Delta\omega)\Delta F \tag{4.8}$$

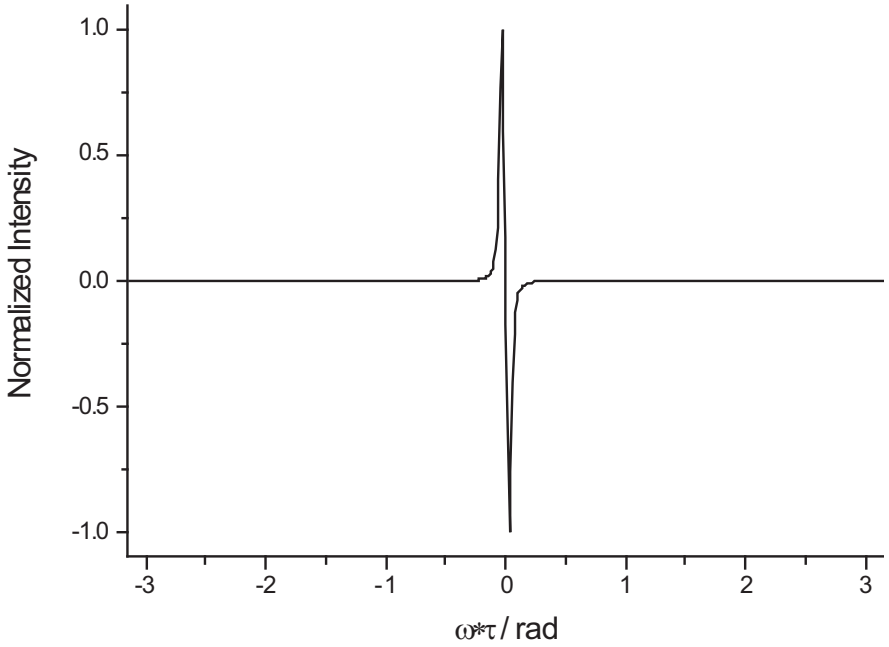

FIG. 4.5: Demodulation curve of hybrid digital serrodyne modulation. Parameters: resonant length L: $10.7m$; shifted frequency Δf: $100kHz$; coupler transmission port loss $(-20\log\lambda_{CT})$: $0.03dB$; fiber one turn transmission loss including splicing loss $(-20\log\lambda_L)$: $0.1dB$; coupler coupling constant κ_C: 0.99.

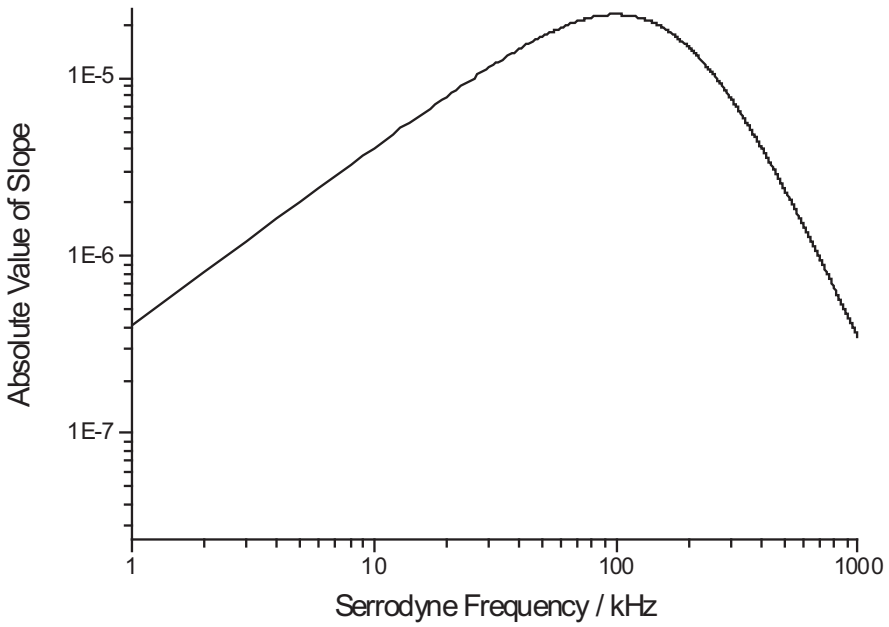

FIG. 4.6: Demodulation sensitivity as a function of shifted frequency. Parameters: resonant length L: $10.7m$; coupler transmission port loss $(-20\log\lambda_{CT})$: $0.4dB$; coupler reflection port loss $(-20\log\lambda_{CR})$: $0.3dB$; fiber one turn transmission loss including splicing loss $(-20\log\lambda_L)$: $0.05dB$; coupler coupling constant κ_C: 0.99.

This results in a current of:

$$\Delta i_{out,f_{rp}} = \frac{e\eta \Delta I_{out,f_{rp}}}{hf} \tag{4.9}$$

where e, η, h, f are the electricity of one electron, quantum efficiency of the photo detector, Prank constant, light wave central frequency, respectively. Besides, the average current when the central frequency is locked is:

$$\overline{i_{out}} = \frac{e\eta}{hf} E_0^2 (\beta - \frac{\gamma}{1-\delta})^2 \tag{4.10}$$

Therefore, the shot noise induced current is:

$$i_n = \sqrt{2eB\overline{i_{out}}} \tag{4.11}$$

where B is bandwidth of the signal processing circuit. By equating Eq. 4.9 with Eq. 4.11, the minimal detectable rotation speed limited by the shot noise is:

$$\Omega_{SN} = \frac{n\lambda}{D}(\beta - \frac{\gamma}{1-\delta})\sqrt{\frac{2Bhf}{\eta}} \frac{(1 - 2\delta\cos\frac{\Delta\omega\tau}{2} + \delta^2)^2}{16\sqrt{P}\beta\gamma\tau(1 + 2\delta\gamma^2 + \gamma^2)\sin\frac{\Delta\omega\tau}{2}} \tag{4.12}$$

where n, D, P are the fiber refractive index, diameter of the sensing coil, input power, respectively. Figure 4.7 shows the shot noise determined sensitivity as a function of the shifted frequency of the hybrid serrodyne modulation. The lower than earth rotation rate sensitivity around the frequency of $110kHz$ demonstrates that this kind of modulation scheme can be used in high grade gyroscopes.

From the above numerical calculations, it can be concluded that the optimized shifted frequency of the hybrid serrodyne modulation is in the range of $100kHz \backsim 120kHz$.

4.2 Effect of Imperfect 2π Voltage of the Phase Modulator

In the previous discussion, we have simply assumed that the digital serrodyne modulation has an amplitude of 2π as in the ideal case. What is the influence of the imperfect modulation voltage? As pointed out in [19], an imperfect 2π voltage of the serrodyne modulation will result in reset pluses at the serrodyne frequency. Since Δf is a harmonic of the repetition frequency f_{rp}, the imperfect digital serrodyne modulation would induce bias drift in synchronous detection.

The causes can be explained by the phaser diagram as shown in Fig. 4.8. The light incident into the photodetector is composed of two electric fields: $\overline{E}_r$ and $\overline{E}_0$. The former is the light coupled out from the resonator. It interferes with the incident field

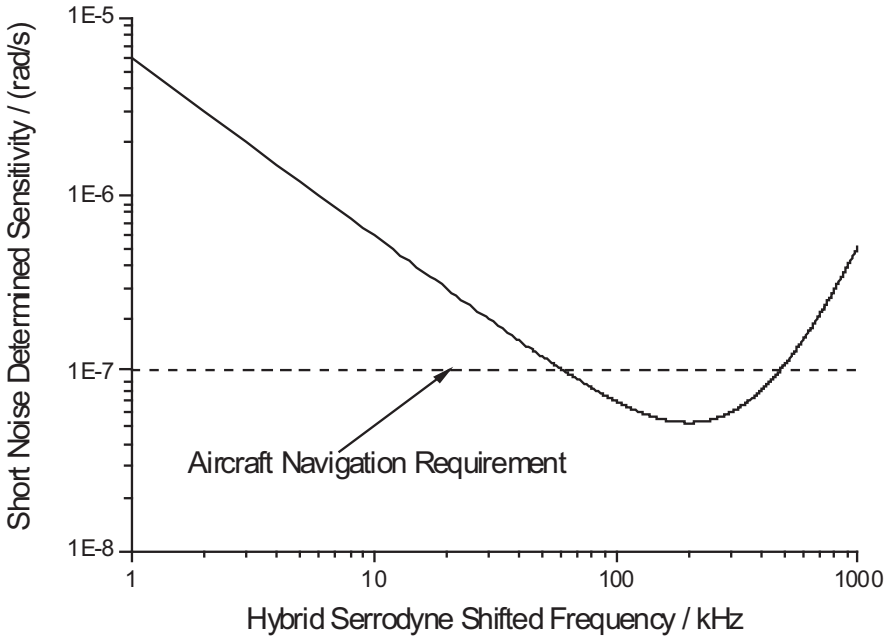

FIG. 4.7: Short noise determined detection sensitivity as a function of shifted frequency. Parameters: resonant length L: $10.7m$; coupler transmission port loss ($-20\log\lambda_{CT}$): $0.4dB$; coupler reflection port loss ($-20\log\lambda_{CR}$): $0.3dB$; fiber one turn transmission loss including splicing loss ($-20\log\lambda_L$): $0.05dB$; coupler coupling constant κ_C: 0.99; input power P: $10mW$; resonator diameter D: $10cm$; signal processing bandwidth B: $0.5Hz$; photo detector quantum efficiency η: 0.6, fiber refractive index n: 1.46.

of $\overline{E}_0$. On the resonant condition, the phases of the two fields are separated by π, which results in the total destructive interference.

When the incident light is reset at a predefined 2π voltage, pulses with different shapes will be observed. For simplicity, the following discussion is based on the assumption that the incident field $\overline{E}_0$ is $\pi/2$ phase ahead of $\overline{E}_r$. When the modulating voltage is the same as $V_{2\pi}$ as shown in Fig. 4.8(a), the transient behavior the phaser $\overline{E}_0$ is that it first passes the total destructive interference phase point and then total constructive interference phase point and finally return to the original starting point. Since the starting and ending point are the same, the output intensities just before and just after the reset pulse are the same. When the 2π voltage is small as in Fig. 4.8(b), the incident electric field is stopped before it can reach the phase of $\overline{E}_0$, which results in an output intensity just after the reset pulse larger than before. Later on, the electric field will approach to the stable state, and the intensity will drop to the original level. Vice versa, the output intensity would be smaller than just before resetting when the 2π voltage is larger than ideal as shown in Fig. 4.8(c). All in all, the smaller than ideal modulation voltage causes a convex pulse and the larger than ideal modulation voltage causes a concave pulse in the output.

Another point that calls for our attention concerning the synchronous detection of

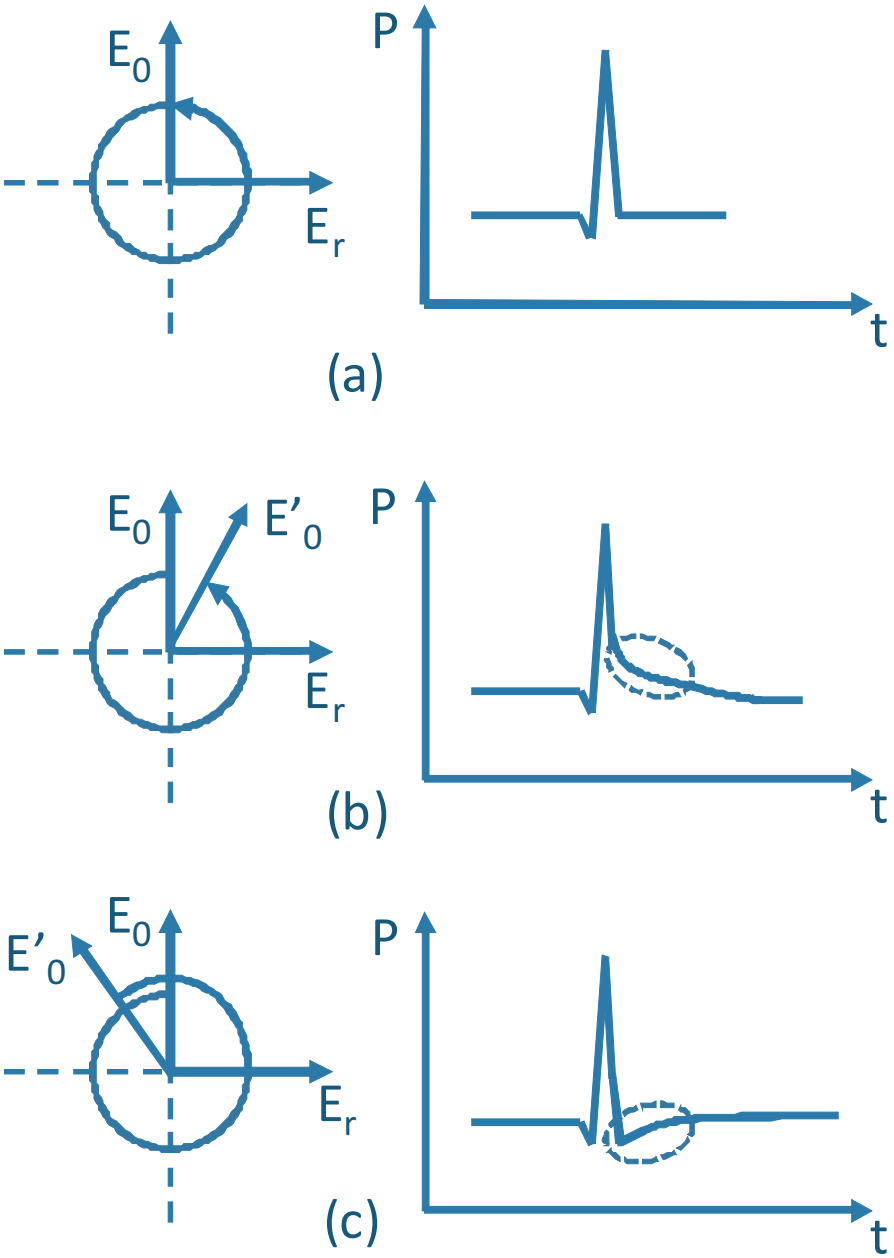

FIG. 4.8: Reset pulses with different digital serrodyne waveform amplitudes : (a) Exact; (b) Too small; (c) Too large.

serrodyne frequency is that in case of backscattering the LIA output is not a true reflection of the imperfect modulation voltage. This is because interference between the unsuppressed carrier component of the backscattered light and the hybrid digital serrodyne signal light is also of frequency Δf. Fortunately, this problem can be automatically solved if we modulate the incident light with the waveform as shown in Fig. 4.2(a). This can be explained by Fig. 4.9. The hybrid digital serrodyne waveform shifts the central frequency of the incident lightwave by $+\Delta f$ in the first half of period. Then it jumps

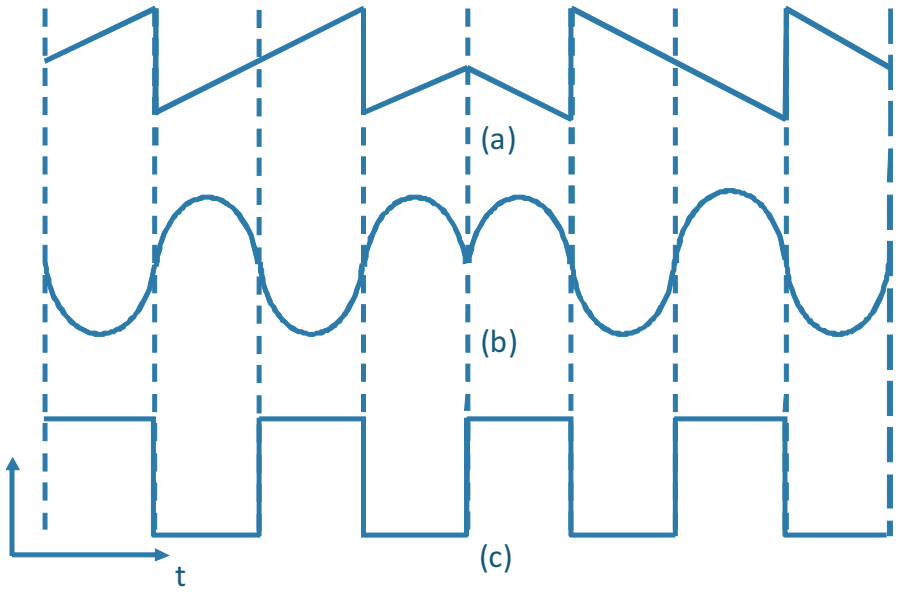

FIG. 4.9: Principle of interference noise reduction by π phase shift. (a) Hybrid digital serrodyne; (b) Interference pattern between the backscattered carrier component and the digital serrodyne modulation waveform; (c)Synchronous detection signal.

to $-\Delta f$ in the second half. This discontinuity in the shifted frequency causes the interference pattern as indicated in Fig. 4.9(b), who has a π phase shift in the middle point. This means if we integrate the interference signal in a total period of time, Fig. 4.9(c) being the synchronization signal, the overall intensity noise is zero. Therefore, even though there might be backscattered carrier component in the signal light path, the influence on the synchronous detection output due to imperfect serrodyne modulation can be removed [3].

4.3 Experiment

In this section, we first experimentally demonstrate the hybrid digital serrodyne modulation and demodulation process based on the discussion above. Then we show the adaptive 2π voltage compensation with the digital controller. Finally, the quasi-rotation measurement with a sensitivity of $0.8^o/s$ is presented.

The experiment setup scheme is depicted in Fig. 4.10. It is featured with the digital controller which is developed to include three feedback loops and one output circuit, all of which are built on the National Instrument (NI) PXI Real Time System running at a speed of $15.1kHz$. The first and the forth loop is used to control the hybrid digital serrodyne waveform amplitude. Instead of controlling the analogue amplification settings of the function generator as traditionally did, which might take up to $50ms$ per time, the digital controller sets a digital gain, which is determined by the Proportional

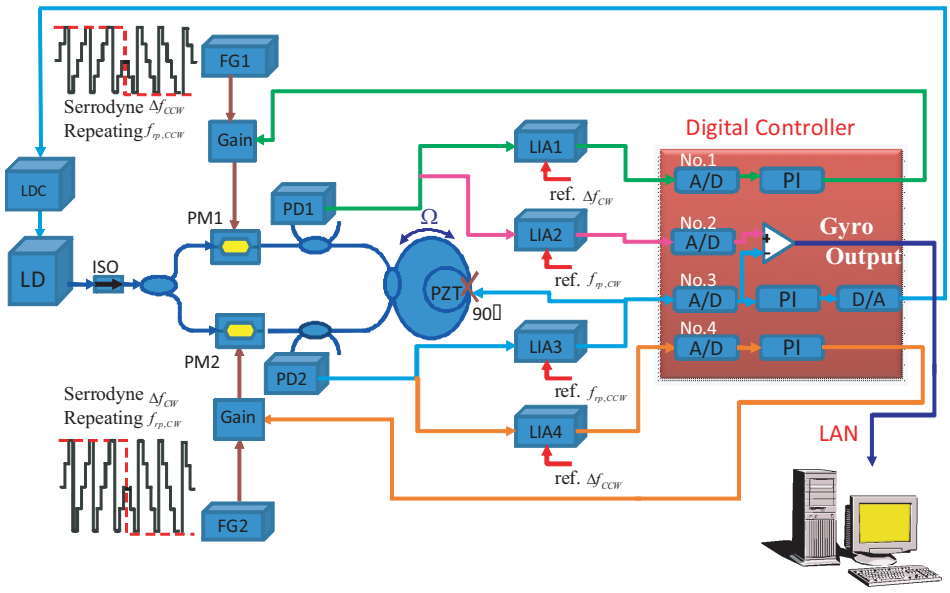

FIG. 4.10: Quasi-rotation experiment setup scheme. LD: laser diode; LDC: laser diode controller; ISO: isolator; PM: phase modulator; FG: function generator; PD: photodetector; LIA: Lock-in Amplifier.

Integration (PI) algorithm, to the NI PXI Arbitrary Function Generator 5422 to amplify or attenuate signals. With this feature, the downloaded waveform samples are scaled by the gain factor digitally before being generated as analog signals. As a result, the amplitude of a given signal can be adjusted in real time. Next, the third loop is used to lock the central frequency of CCW lightwave to that of the laser diode. Besides, an additional analogue signal is feeded back to the PZT to track high frequency drifts, this can be integrated into the digital controller if a FPGA module with a faster processing speed is used. What's more, the gyro output is generated by the voltage difference between the second and the third circuit. As stated in [3], this can also be used as the trigger signal in the closed loop operation. Finally, the output is loaded to the local computer through the LAN. To separate the algorithm problem from the fiber optical system instability, the algorithms are compiled in a separate PMF based R-FOG system.

4.3.1 Demodulation with Hybrid Digital Serrodyne Waveform

We first scan the LD with a sawtooth waveform to retrieve the resonant curve. The finesse and the fiber length is calculated to be 59 and 10.7m, respectively. As stated in [4], the demodulation curve is of highest sensitivity when the step duration of digital serrodyne waveform equals to the one turn transmission time. In other words, the sampling rate of the arbitrary function generator should be set to that of one FSR, which is 19.24$Msamples/s$ in this case.

A finesse of 59 indicates a one turn loss of around $0.46dB$, which, according to Fig. 4.5 and Fig. 4.6, has the best performance when the shifted frequency Δf is in the range of $100kHz \backsim 120kHz$. This frequency is related to the sampling rate of the function generator by:

$$\Delta f = \frac{f_{FG}}{n_s} \tag{4.13}$$

where, f_{FG} and n_s are the sampling rate of the function generator and the number of samples in one serrodyne period.

To get rid of the influences of the backscattered light, not only the shifted frequency of the CW side (Δf_{CW}) and the shifted frequency of the CCW side (Δf_{CCW}) should be different but also their higher harmonics should not superpose each other. In other words, the generated waveforms should not overlap with one another as long as possible. This can be satisfied if n_s is chosen to be a prime number. However, according to the manual of NI PXI Arbitrary Function Generator 5422, the number of samples that each waveform contains should be an integer times of 4. Thus, we choose 4 times a smaller prime number as the sampling points in one serrodyne waveform. Taken the above requirements into considerations, $n_{s,CCW}$ and $n_{s,CW}$ are set to $4 \times 47 = 188$ and $4 \times 43 = 172$, respectively. This corresponds to a shifted frequency of $102.3kHz$ in the CCW side and $111.9kHz$ in the CW side.

When designing the repetition frequency, that is to say the number of serrodyne periods it contains in one hybrid digital serrodyne waveform, two points are considered: (1) the first half is symmetric to the second half; (2) the number of serrodyne periods in each half n_{rp} is also a prime number. Therefore, the repetition frequency is:

$$f_{rp} = \frac{f_{FG}}{2n_s n_{rp}} \tag{4.14}$$

In this experiment, we choose $n_{rp,CCW} = 5$, $n_{rp,CW} = 7$. This equals to $f_{rp,CCW} = 10.23kHz$ and $f_{rp,CW} = 7.99kHz$.

To synchronously detect the imperfect 2π output from the LIA, synchronization signals with frequency of Δf_{CCW} and of Δf_{CW} are required. At first, we supplied the LIA with a signal that is generated by low pass filtering the hybrid digital serrodyne modulation signal. However, it was found that the LIA met with the "UNLOCK" problem due to the π phase shift in the middle point of the waveform. This was solved by using the so-called "Marker Event" technique available in NI PXI 5422 arbitrary waveform generator. With a marker event, the state of trigger lines will change synchronously with the generation of a specific sample. Figure 4.11 depicts the generated hybrid digital serrodyne modulation waveform for the CCW side and its synchronization signal.

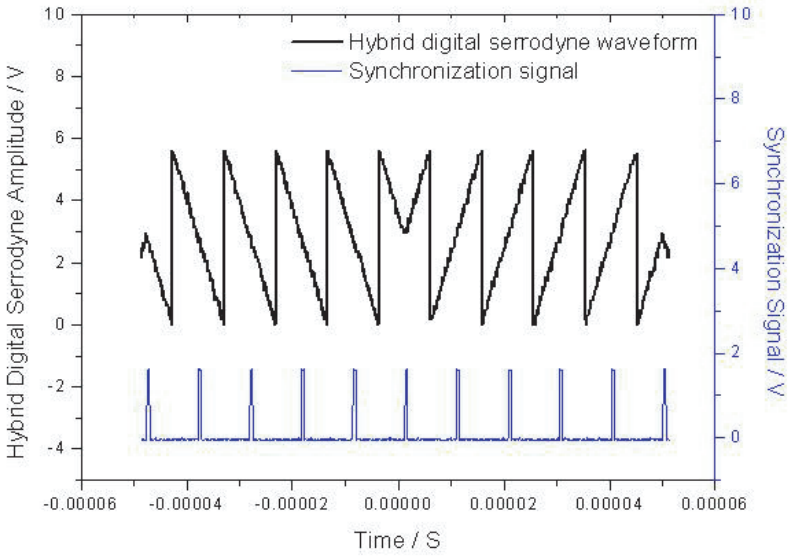

FIG. 4.11: Generated hybrid digital serrodyne modulation waveform and the synchronization signal.

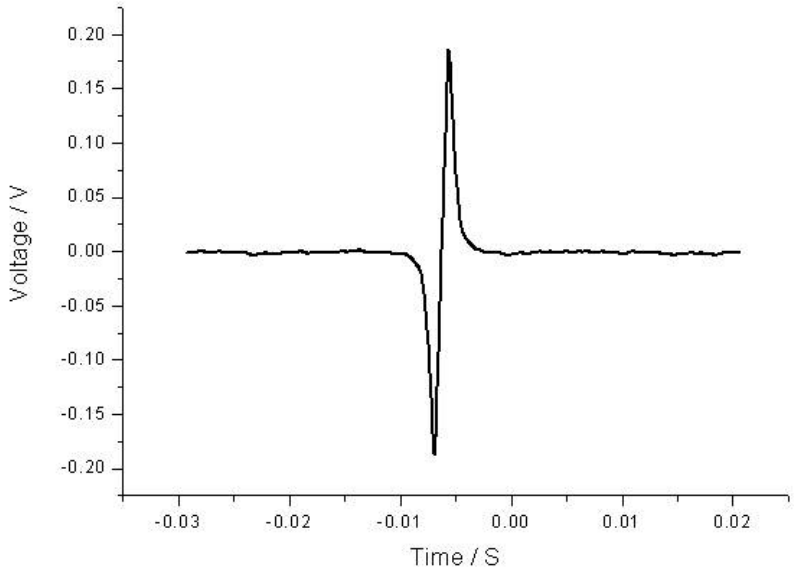

FIG. 4.12: Demodulation curve with the hybrid digital serrodyne modulation.

The demodulation curve is shown in Fig. 4.12. The time constant and the slope of the Lock-in Amplifier are $300\mu s$ and $24dB$, respectively. Finally, it is calculated from the demodulation curve that the scale is $1.2kHz/mv$.

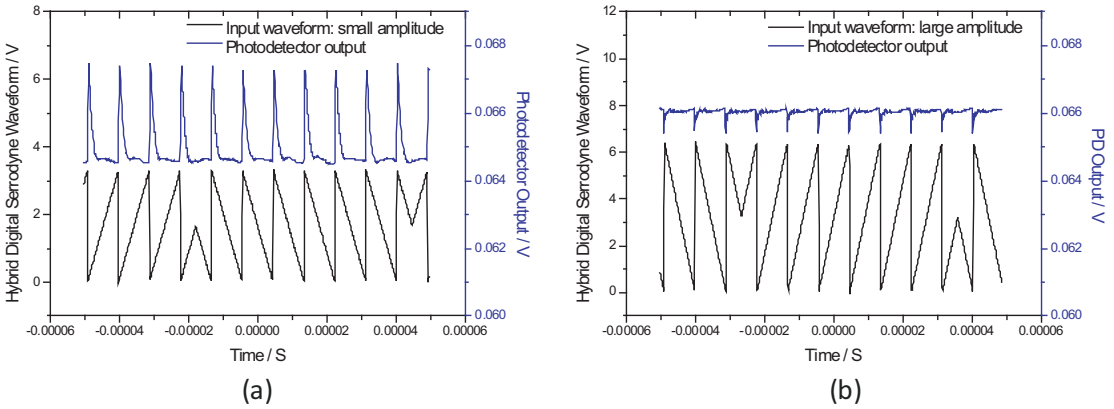

FIG. 4.13: Transient behavior of photodetector output with hybrid digital serrodyne modulation of different amplitude: (a) $3.4V$, (b) $6.3V$.

4.3.2 Adaptive Compensation of Phase Modulator $V_{2\pi}$

To demonstrate the idea that imperfect modulation waveform produces different transient tails according to the amplitude level, two input voltages are arbitrarily selected: $3.4V$ and $6.3V$. The frequency parameters are the same as in the previous experiment. Besides, the third feedback loop is on to track the LD central frequency. The output is obtained directly from the photodetector. The result is shown in Fig. 4.13.

According to later experiment results, $3.4V$ is smaller than the ideal 2π voltage of the phase modulator while $6.3V$ is too large. The results fit well with the previous conclusion that small voltage produces a convex tail while large voltage generates a concave tail.

Next, the synchronous detection with different input voltages is examined. The voltage is increased from $5.4V$ to $6.0V$ by 0.5V per step. The LIA is synchronized to the serrodyne frequency generated by the "Marker Event" technique. The result is displayed in Fig. 4.14. This graph indicates that the synchronous detection with the serrodyne frequency is linearly related to the amplitude of modulation waveform, which makes the PI feedback possible.

To automatically compensate for the 2π voltage drift of the phase modulator, the first and the forth loop are incorporated into the digital controller as shown in Fig. 4.10. The LIA output is sampled by the A/D converter at a sampling rate of $15.1kHz$. The sampled digital number is fed into the PI algorithm:

$$\begin{aligned} u(k) &= u_P(k) + u_I(k) \\ &= K_c[e(k) + \frac{1}{T_i}\sum_{i=1}^{k}\frac{e(i)+e(i-1)}{2}\Delta t] \end{aligned} \tag{4.15}$$

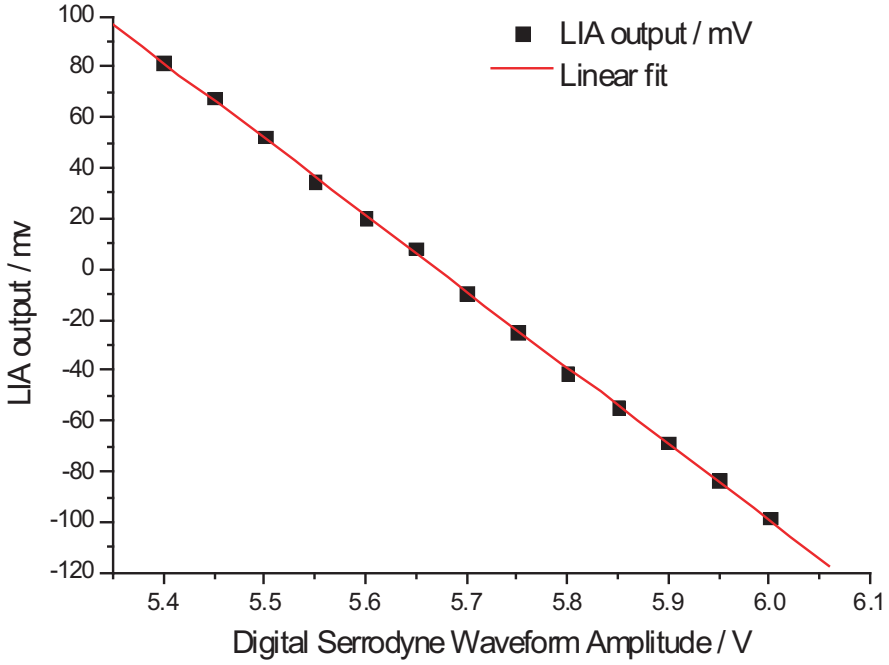

FIG. 4.14: Synchronous detection of the serrodyne frequency as a function of modulation amplitude.

where $u(k)$, $u_P(k)$, $u_I(k)$, $e(k)$, K_c, T_i, and Δt stand for the total output, the output due to proportional action, the output due to integration action, the error, the gain, the integration time and the loop period, respectively. The output is transferred to the digital gain controlling part of the function generator, which updates its value when the next loop starts. Since the whole process is handled by the PXI system, it runs at a much faster speed than the traditional system based on the GPIB communication.

Figure 4.15 records the Lock-in Amplifier output before and after the feedback loop is turned on. From this figure we can conclude that the digital controller finally found the appropriate 2π voltage of the phase modulator that brought the LIA output to $0V$.

Finally, we checked the photodetector output when the modulation amplitude is set to the appropriate value, which is $5.68V$ in this experiment. By comparing Fig. 4.16 with Fig. 4.13, it can be concluded that this scheme is effective in reducing the imperfect 2π voltage induced noise.

4.3.3 Quasi-Rotation Measurement

With the first, the third and the forth loop on, we detected the quasi-rotation signal from the output port of the second circuit. The incident CCW lightwave is modulated at PM1 with a shifted frequency of $\Delta f_{CCW} = 102.3kHz$ and a repetition frequency of $f_{rp,CCW} = 10.23kHz$. To lock the central frequency of the laser diode, the $f_{rp,CCW}$

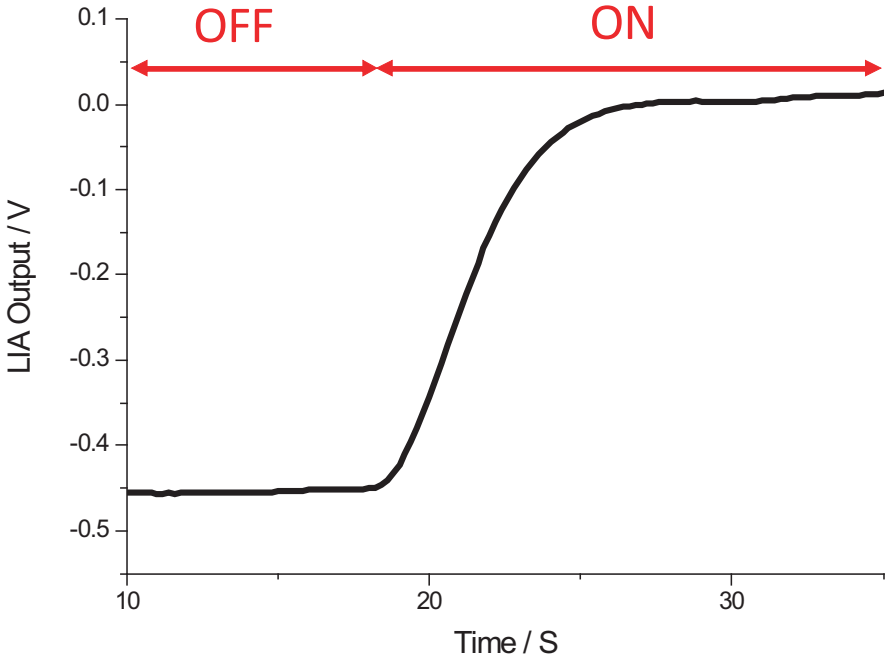

FIG. 4.15: Lock-in amplifier output before and after the 2π voltage feedback loop on.

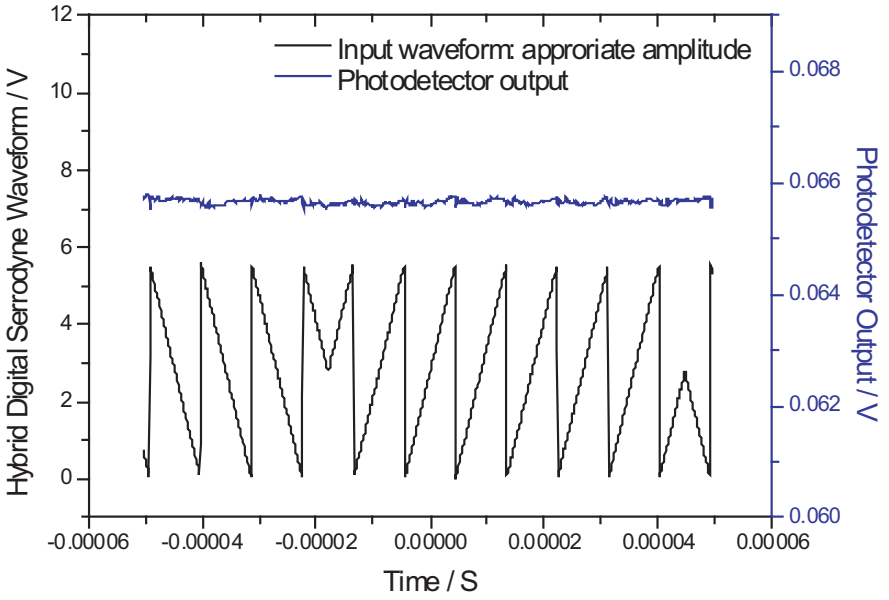

FIG. 4.16: Photodetector output when the 2π voltage of the phase modulator is reached.

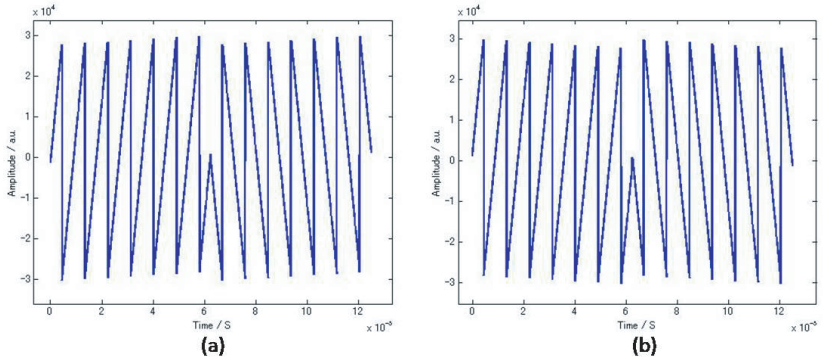

FIG. 4.17: Hybrid digital serrodyne waveform with additional central frequency shift: (a) up-shift; (b) down-shift.

component in the PD2 output is used as the input to the feedback loop $No.3$, with the time constant of LIA3 being $10ms$. The analogue signal after the PI calculation of the third loop is sent back to the laser diode controller with a modulation bandwidth of $30kHz$ to cancel out the slow drift of the laser diode central frequency. Meanwhile, the analogue output of LIA3 is also connected to the PZT to track the fast changes.

On the other hand, the CW wave is modulated at PM2 by the hybrid digital serrodyne with additional central frequency shift to emulate the rotation. The base waveform has a shifted frequency of $\Delta f_{CW} = 111.9kHz$, and a repetition frequency of $f_{rp,CW} = 7.99kHz$. The added linear waveform shifts the central frequency by another $+0.65kHz$ with a positive slope and $-0.65kHz$ with a negative slope. This is realized by adding or subtracting 2 Least Significant Bits (LSBs) from each step of the base waveform, whose step height is 340LSBs. The generated waveform is recorded in Fig. 4.17, with the unit of Y axis being "LSB". According to Eq. 2.1, this equals to a rotation speed of $0.8^o/s$.

Traditionally, to generate the modified version of the modulation signal, at least two function generators are needed. Now, this can be realized by just one. We first program the three waveforms that will be generated: base, upshifted, down shifted, and download them to the memory of the function generator. Next we define the order and the number of iteration of each waveform. Then we can obtain the desired time sequence when the loop begins to work.

The quasi-rotation result is shown in Fig. 4.18. This is obtained by subtracting the digitalized voltage output of LIA2 from that of LIA3. The problem that the output voltage does not equal to zero when the R-FOG is at rest might result from the quantization error in the A/D and D/A process in the third feedback loop. This might be reduced if a digitizer with more bits is used. Besides, the result of $0.8^o/s$ fits well with that calculated from the $0.65kHz$ frequency shift.

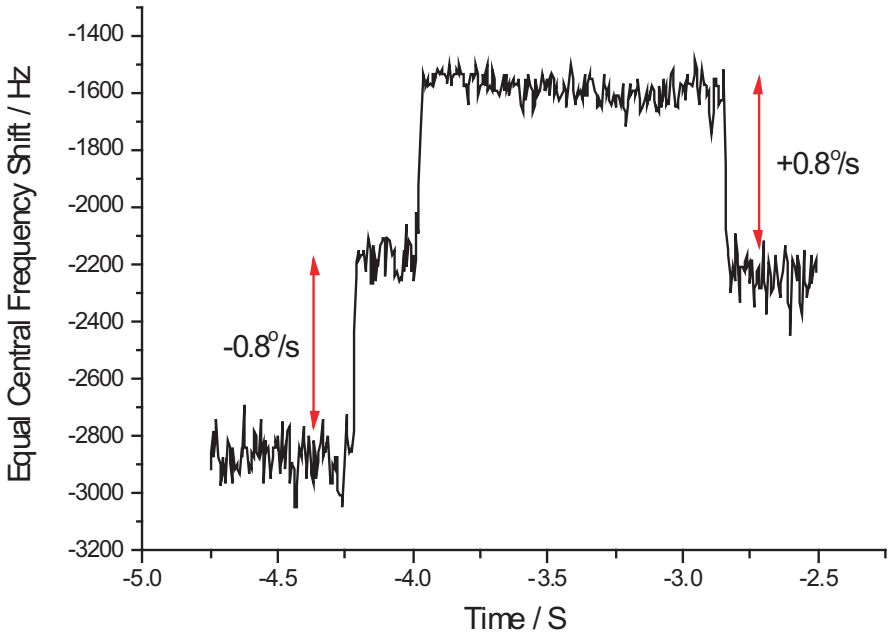

FIG. 4.18: Quasi-rotation measurement result.

4.4 Conclusion

We experimentally demonstrate the quasi-rotation measurement of the R-FOG, where a digital controller is newly developed to track the laser diode central frequency drift and to compensate the 2π voltage of the phase modulator based on the reset pulse amplitude of digital serrodyne modulation. The digital processor can be designed with much higher flexibility and simplicity compared with traditional analogue circuits. By incorporating modules with higher processing power, we are expecting to build an R-FOG that is totally digitalized.

Chapter 5

Polarization Problem Treatment by Twice 90^o Rotation Splicing

This chapter deals with the polarization problem in the R-FOG. The twice 90^o polarization-axis rotation method is adopted as the anti-measurement. A new model which takes the crosstalk at the coupler into consideration is analyzed. This model is also featured with the double-coupler configuration that avoids the use of polarizers at the output ports. Numerical results show that this method can achieve the aircraft-navigation requirements by adjusting the resonator parameters.

5.1 Polarization Problem in the R-FOG

Polarization induced error due to birefringence remains as one of the major problems in the R-FOG. Each of the two polarization modes, called ESOPs [7], propagates through the ring with slightly different optical length, which results in two sets of resonance. Besides, these two peaks/dips drift across each other in a varying temperature environment as demonstrated in Fig. 5.1. In previous discussion, we have simply assumed that only one of the ESOPs are excited. As a matter of fact, the second ESOP can be easily excited without intricate polarization condition control. What is worse, the excited unwanted ESOP drifts with respect to that of the main dip as the birefringence in the loop changes. This is especially true for a PMF sensing coil, which is temperature sensitive.

Several solutions have been proposed previously. In [9], it is recommended that the sensing fiber is 90^o rotation spliced at the middle point. This is effective in settling the two ESOPs π phase away from each other at the expense of always exciting both ESOPs

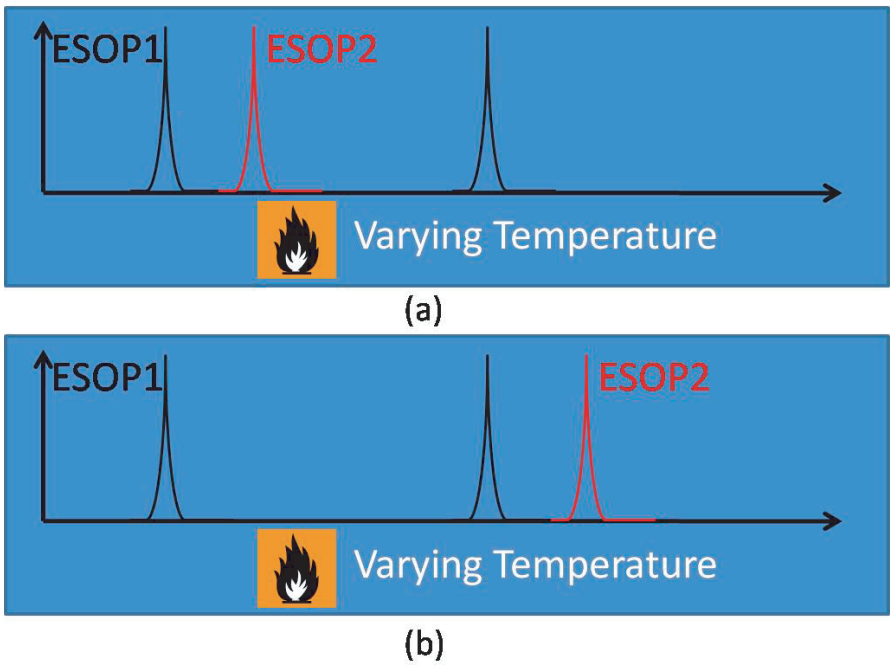

FIG. 5.1: Two ESOPs drift across each other in a varying temperature environment.

at similar level. Another possibility might be introducing anisotropic behavior between the two ESOPs as suggested in [20]. However, this might suffer from the large loss inside the ring, which reduces the Finesse greatly.

Another possible solution might be twice 90^o rotation splicing. In the ideal case of no misalignment at each of the splice, the ESOPs are the same as the $x-$ and $y-$ axes of the polarization maintaining fiber. Moreover, if the phase difference between the two ESOPs is π, the ESOPs are two linear polarizations close to the two axes. Under this situation, we can selectively excite only one of them. Although the theoretical analysis has been carried out in [21], the crosstalk of the coupler is ignored. However, as pointed out in [22], one of the major sources of crosstalk in the ring resonator occurs in the coupler. Besides, better system performance is expected by removing the polarizers at the output ports. Therefore, in the following sections, we will investigate a model that takes the crosstalk of the coupler into consideration while leaves out the polarizers at the exit.

5.2 Mathematical Model

In this section, the twice 90^o splicing method as a treatment of the polarization problem is theoretically discussed. Besides, since both ESOPs are linear when π phase separated, two polarizers just before the resonator are also included. The schematic diagram

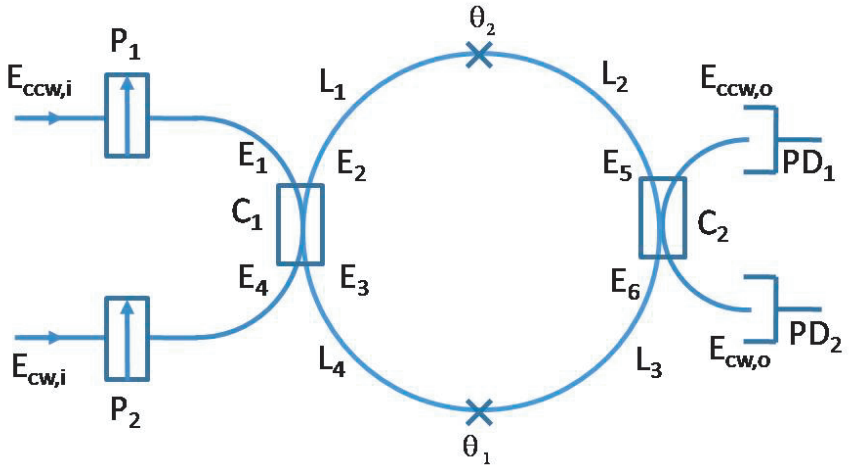

FIG. 5.2: Proposed mathematical model of twice 90^o rotation splicing. $E_{ccw,i}$: input electronic field of CCW side; $E_{cw,i}$: input electronic field of CW side; $E_{ccw,0}$: output electronic field of CCW side; $E_{cw,0}$: output electronic field of CW side; $C_{1,2}$: coupler1, and coupler2; $P_{1,2}$: polarizer1 and polarizer2; $L_{1,2,3,4}$: fiber length; $\theta_{1,2}$: rotation angle; $PD_{1,2}$: photodetector1 and photodetector2.

showing the mathematical model is depicted in Fig. 5.2.

5.2.1 *Jones* Matrices of Optical Components

The diagonal *Jones* matrices describing the coupler without crosstalk are:

$$C_{t,i} = \begin{bmatrix} \sqrt{(1-\gamma_{x,i})(1-\kappa_{x,i})} & 0 \\ 0 & \sqrt{(1-\gamma_{y,i})(1-\kappa_{y,i})} \end{bmatrix} \tag{5.1}$$

$$C_{c,i} = j \begin{bmatrix} \sqrt{(1-\gamma_{x,i})\kappa_{x,i}} & 0 \\ 0 & \sqrt{(1-\gamma_{y,i})\kappa_{y,i}} \end{bmatrix} \tag{5.2}$$

where subscripts $i = 1, 2$; c and t denote coupling and transmission; $\gamma_{x,y}$ the intensity loss coefficients for the $x-$ and $y-$ polarized modes; $\kappa_{x,y}$ the coupling constants, respectively.

For simplicity, the crosstalk in the coupler is modeled by an equivalent misalignment angle θ_d between the fiber axes as shown in Fig. 5.3. It can be described by:

$$A_i = \begin{bmatrix} \cos\theta_{d,i} & -\sin\theta_{d,i} \\ \sin\theta_{d,i} & \cos\theta_{d,i} \end{bmatrix} \tag{5.3}$$

where $i = 1, 2$. The corresponding crosstalk by $\theta_{d,i}$ is $CT_i = 20\log\tan\theta_{di}$.

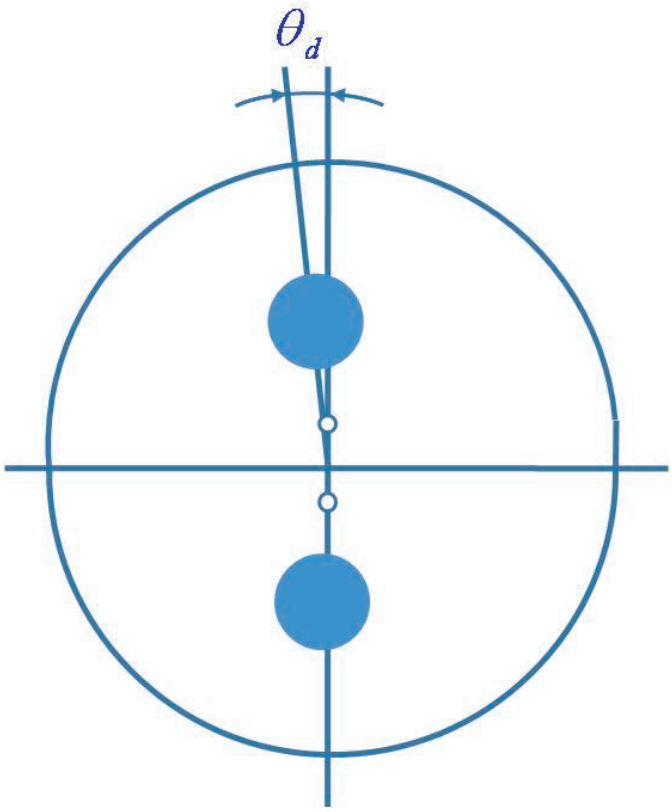

FIG. 5.3: Configuration of the coupler in the R-FOG with crosstalk.

The polarizer with extinction ratio of ϵ_i $(i = 1, 2)$ is:

$$P_i = \begin{bmatrix} 1 & 0 \\ 0 & \epsilon_i \end{bmatrix} \tag{5.4}$$

Moreover, suppose the propagation constant and loss for the slow and fast polarization are $\beta_{x,y}$ and $\alpha_{x,y}$, respectively. The transmission matrix of a section of fiber, with a length of z is:

$$F(z) = e^{-\alpha_{av}z} e^{j\beta_{av}z} \begin{bmatrix} e^{\Delta\alpha z} e^{j\Delta\beta z} & 0 \\ 0 & e^{-\Delta\alpha z} e^{-j\Delta\beta z} \end{bmatrix} \tag{5.5}$$

where $\beta_{av} = (\beta_x + \beta_y)/2$, $\Delta\beta = (\beta_x - \beta_y)/2$, $\alpha_{av} = (\alpha_x + \alpha_y)/2$ and $\Delta\alpha = (\alpha_x - \alpha_y)/2$. By these parameters, the birefringence and polarization dependent loss behavior of PMF can be determined.

The axis rotation effect at each of the splicing point can be described as:

$$R(\theta_i) = \begin{bmatrix} \cos\theta_i & -\sin\theta_i \\ \sin\theta_i & \cos\theta_i \end{bmatrix} \tag{5.6}$$

where the subscript $i = 1, 2$.

Combining the above equations, the one turn transmission matrix for the CCW side is:

$$S_{CCW} = A_1 C_{c,1} F(L_1) R(\theta_1) F(L_2) A_2 C_{c,2} F(L_3) R(\theta_2) F(L_4) \tag{5.7}$$

The transmission matrix for the CW side is:

$$S_{CW} = A_1^{-1} C_{c,1} F(L_4) R(\theta_2)^{-1} F(L_3) A_2^{-1} C_{c,2} F(L_2) R(\theta_1)^{-1} F(L_1) \tag{5.8}$$

5.2.2 Electronic Field Description

Suppose that the input CCW electronic field with unit intensity is:

$$E_{ccw,i} = \begin{bmatrix} \cos\theta_{ccw} \\ \sin\theta_{ccw} e^{j\delta_{ccw}} \end{bmatrix} \tag{5.9}$$

When it arrives at the input port of coupler1, it becomes:

$$E_1 = P_1 E_{ccw,i} \tag{5.10}$$

The transmission of the resonator can be seen as the multi-interference of the electronic fields coupled out of the resonator:

$$\begin{aligned} E_3 &= (1 + S_{ccw} + S_{ccw}^2 + S_{ccw}^3 + \dots) C_{t,3} E_1 \\ &= D_{ccw} C_{t,3} E_1 \end{aligned} \tag{5.11}$$

where $D_{ccw} = \sum_{n=0}^{\infty} S_{ccw}$

Additionally, $E_{ccw,o}$ and E_3 are related by:

$$E_{ccw,o} = M_{ccw} E_3 \tag{5.12}$$

where $M_{ccw} = C_{t,2} F(L_3) R(\theta_2) F(L_4)$.

5.2.3 Eigenvector and Eigenvalue of R-FOG

The ESOPs represent those states of polarization that reproduce themselves after one pass around the loop. According to [7], the behavior of the ESOPs are totally determined by the eigenvectors and eigenvalues of the one turn transmission matrix S as defined in Eq. 5.7. Assume that the eigenvectors of the CCW side are $V_{ccw} = [v_{ccw,1}, v_{ccw,2}]$ and the eigenvalues $\lambda_{1,2} = g_{1,2} e^{\phi_{1,2}}$, where $g_{1,2}$ and $\phi_{1,2}$ are the amplitude and phase of the

eigenvalues. In the physical world, $g_{1,2}$ and $\lambda_{1,2}$ stand for the round trip losses and round trip phase shifts. Besides, the phase difference between the two eigenvalues indicates how far away the two resonant peaks is from each other. S, λ and V are related by:

$$S_{ccw}V_{ccw} = \lambda_{i,ccw}V_{ccw} \quad (i = 1, 2) \tag{5.13}$$

The input field into the resonator is projected onto the two ESOPs:

$$C_{t,3}E_1 = \rho_{ccw,1}v_{ccw,1} + \rho_{ccw,2}v_{ccw,2} \tag{5.14}$$

The weighting factors $\rho_{ccw,1}$ and $\rho_{ccw,2}$ tell the level of the excited ESOPs.

Recalling Eq. 5.13, apply it to the matrix D_{ccw}:

$$\begin{aligned} D_{ccw}v_{1,2} &= (1 + S_{ccw} + S_{ccw}^2 + \dots)v_{1,2} \\ &= (1 + \lambda_{1,2} + \lambda_{1,2}^2 + \dots)v_{1,2} \end{aligned} \tag{5.15}$$

Assume:

$$M_{ccw}^{+}M_{ccw} = \begin{bmatrix} m_{ccw,1} & m_{ccw,2} \\ m_{ccw,3} & m_{ccw,4} \end{bmatrix} \tag{5.16}$$

where $^+$ stands for the conjugate transpose.

Substitute this into Eq. 5.12:

$$\begin{aligned} |E_{ccw,o}|^2 = &\frac{|\rho_{ccw,1}|^2}{|1-\lambda_{ccw,1}|^2}[(m_{ccw,1}+m_{ccw,3})|v_{ccw,1x}|^2 + (m_{ccw,2}+m_{ccw,4})|v_{ccw,1y}|^2] \\ &+ \frac{|\rho_{ccw,2}|^2}{|1-\lambda_{ccw,2}|^2}[(m_{ccw,1}+m_{ccw,3})|v_{ccw,2x}|^2 + (m_{ccw,2}+m_{ccw,4})|v_{ccw,2y}|^2] \\ +2Re\{&\frac{\rho_{ccw,1}^*\rho_{ccw,2}}{(1-\lambda_{ccw,1}^*)(1-\lambda_{ccw,2})}[(m_{ccw,1}+m_{ccw,3})v_{ccw,1x}^*v_{ccw,2x} + (m_{ccw,2}+m_{ccw,4})v_{ccw,1y}^*v_{ccw,2y}]\} \end{aligned} \tag{5.17}$$

where * stands for the complex conjugate. Similar expression for the CW side can be written out with simple algebra calculations.

It should be noted that while it is true that in an isotropic resonator without polarization dependent loss, whose two ESOPs are orthogonal to each other ($v_1^+v_2 = 0$), the interference term disappears; in an anisotropic resonator, such as the situation we modeled, this term will remain, which results in bias drift in the R-FOG. This can be explained by Fig. 5.4.

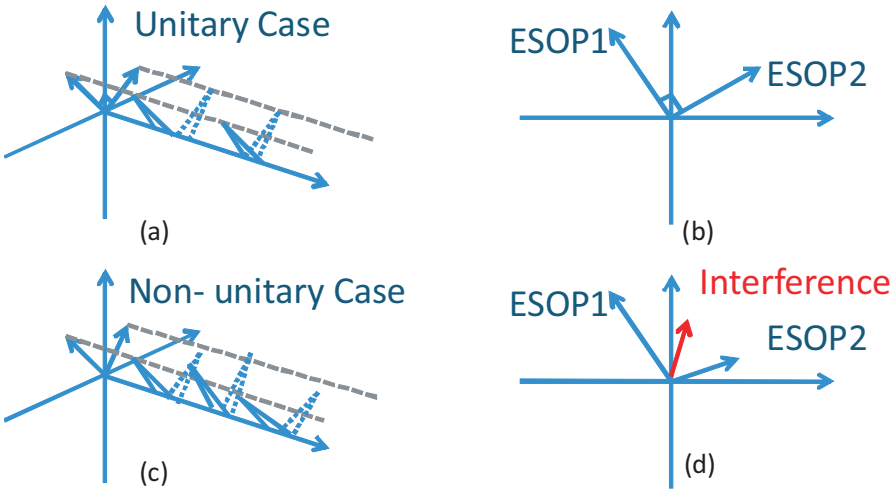

FIG. 5.4: Demonstration of two ESOPs propagate simultaneously through the fiber: (a) unitary case; (b) two ESOPs after one round trip in unitary case; (c) non-unitary case; (d) two ESOPs after one round trip in non-unitary case.

5.2.4 Demodulation Error Caused by Polarization Problem

Suppose that the CW side is used to lock the LD central frequency, and the resonant frequency of the CCW side is used to read out the rotation signal. Besides, the digital serrodyne modulation technique is used, with f_{rp} component in synchronous detection being $C(f) = I_{out,f_{rp}}(f + \Delta f) - I_{out,f_{rp}}(f - \Delta f)$.

For the CCW and CW sides, the detected resonant frequencies $f_{ccw,0}$ and $f_{cw,0}$ are:

$$\begin{aligned} C_1(f_{ccw,0}) + C_2(f_{ccw,0}) + C_3(f_{ccw,0}) &= 0 \\ C_1(f_{cw,0}) + C_2(f_{cw,0}) + C_3(f_{cw,0}) &= 0 \end{aligned} \tag{5.18}$$

where $C_{1,2,3}$ correspond to resonance output by ESOP1, ESOP2 and their interference.

Therefore, the polarization drift induced error is:

$$\Omega_{error} = \frac{n\lambda}{D}(f_{ccw,0} - f_{cw,0}) \tag{5.19}$$

where n, λ, D are the refractive index, the wave length, diameter of the sensing coil, respectively.

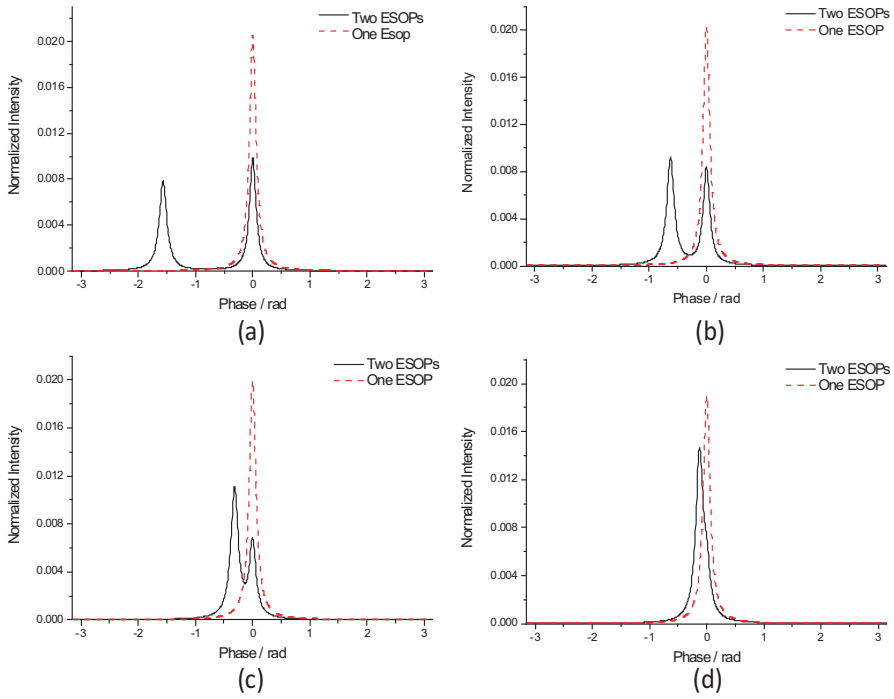

FIG. 5.5: Resonant curves when two ESOPs are excited. The phase difference: (a)0.5π, (b)0.2π, (c)0.1π, (d)0.04π. Parameters: coupler1, 2 $x-$ polarization loss: $0.2dB$; $y-$ polarization loss: $0.2dB$; $\kappa_{x,i} = 0.99$; $\kappa_{y,i} = 0.99$ (i=1,2); $CT_{1,2} = -20dB$ ($\theta_d = 0.1rad$); beat length: $3mm$; fiber transmission loss $0.3dB/km$ for x polarization and $0.4dB/km$ for y polarization. This corresponding to a finesse of 88. In initial condition, $L_1 = L_2 = L_3 = L_4 = 2.5m$. The rotation angle of each splicing point is set to 90^o.

5.3 Numerical Analysis

5.3.1 Numerical Simulation

In this section, we will give some numerical examples to show how each of the parameters influence the R-FOG output.

First, we give the resonant curves when two ESOPs are simultaneously excited. To simulate the worst case, the couplers polarizers $P_{1,2}$ are removed and the input electronic field is 45^o linearly polarized. The results are shown in Fig. 5.5. It is clear that as the two ESOPs are more and more approaching each other, the observable central frequency is shifted away from that of only one ESOP being excited. If one of them moves across the other from time to time, large bias drift would appear at the output port.

Another direct way to see how the double ESOPs causes error in the R-FOG output is from the demodulation curve as in Fig. 5.6. The parameters are the same as those used in the previous one. This demonstrates the "adding up" effect of the two ESOPs in demodulation. The worst case happens when the phase difference is close to zero.

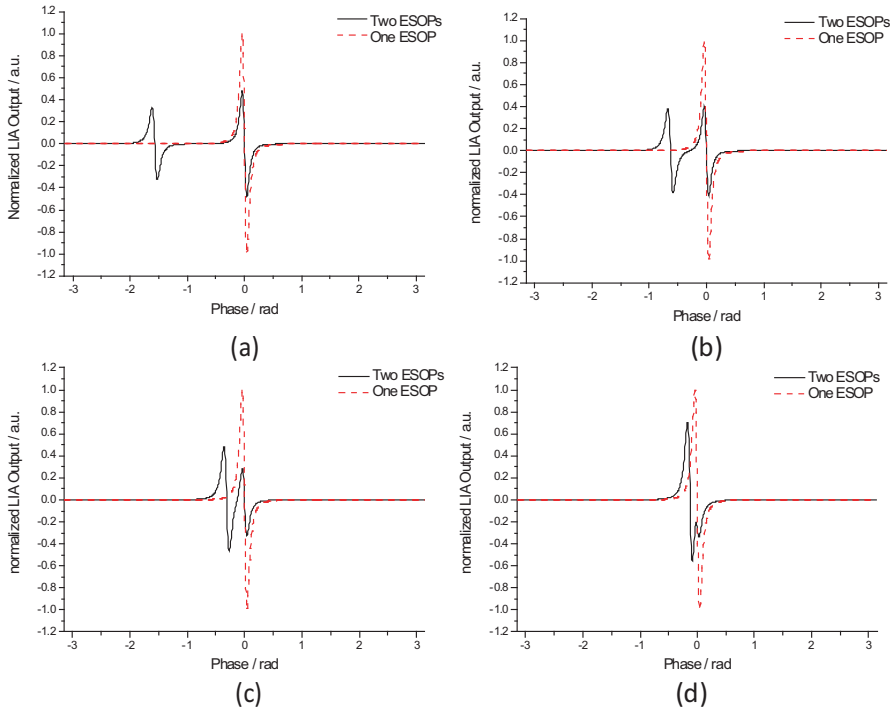

FIG. 5.6: Demodulation output when two ESOPs cross each other. The phase difference: (a)0.5π, (b)0.2π, (c)0.1π, (d)0.04π.

Next, we will numerically show demodulation error as a function of one turn phase difference between the two ESOPs. Parameters include the polarizer extinction ratio, the coupler crosstalk, coupler coupling constant, rotated angle at the splicing point, the state of polarization of the input electronic field and the finesse.

(1) Demodulation error with different polarizer extinction ratio

Figure 5.7 and Fig. 5.8 show the demodulation error as a function of phase difference with polarizer extinction ratio as the parameter. The related parameters are listed in Table 5.1 and Table 5.2, respectively. It can be concluded that even polarizers with medium performance of $30dB$ polarization extinction are included, the bias error can be reduced by up to three orders when the ESOPs are separated by a phase of π. Therefore, polarizers at the entrance should be considered as one of the anti-measurements of the polarization induced bias drift in R-FOG. On the other hand, polarizers at the output port degrades the system performance a lot, which verifies our proposal that better system performance can be achieved if polarizers at the output ports are removed. Under this situation, the additional transfer matrix M_{ccw} and M_{cw} can be written as:

$$\begin{aligned} M_{ccw} &= P_3 C_{t,2} F(L_3) R(\theta_2) F(L_4) \\ M_{cw} &= P_4 C_{t,2} F(L_2) R(\theta_1)^{-1} F(L_1) \end{aligned} \tag{5.20}$$

where $P_{3,4}$ are the *Jones* matrices of the polarizers before photodetector1 and photodetector2, respectively. From the simulation result, the output error is above the aircraft navigation requirement even if the phase difference between the two ESOPs is π. This can be explained as that in an anisotropic ring resonator, the eigenvectors are not orthogonal to each other, and their interference will results in bias drift in the output. Finally, the smaller the misalignment angle, the higher the sensitivity. This could be explained as the smaller the misalignment angle the closer the ESOPs being to the $x-$ and $y-$ axis when π phase separation is reached.

(2) Demodulation error with different coupler crosstalk

Figure 5.9 and Fig. 5.10 show the demodulation error as a function of phase difference between the two excited ESOPs with the crosstalk in coupler as the parameter. Other parameters used in the simulation are listed in Table 5.3 and Table 5.4. It is quite clear that this parameter has a large influence on the system performance. And it is a more realistic model to consider the crosstalk than the previously reported one where this parameter is totally ignored. Besides, couplers with smaller crosstalk perform better in this system. This is because the smaller the crosstalk the higher percentage of the energy is maintained in the wanted ESOP and the closer the eigen state of polarization to the polarization axes of the fiber.

(3) Demodulation error with different coupler coupling constant

The coupling constant for $x-$ and $y-$ polarization $\kappa_{x,y}$ is another important parameter for the coupler. In this simulation, we demonstrate how $\kappa_{x,y}$ influences the bias error induced by polarization drift. The result is shown in Fig. 5.11 and Fig. 5.12. Parameters used in the simulation are listed in Table 5.5 and Table 5.6. From the results, we can conclude that lower coupling constant will degrade the performance because of reduced finesse. Moreover, by increasing the coupling constant in the $y-$ polarization, the bias error will be reduced since smaller part of the electronic filed in the $y-$ direction will be coupled out of the coupler.

(4) Demodulation error with different splicing rotation error

Figure 5.13 and Fig. 5.14 show the demodulation error as a function of phase difference with splicing rotation angle as the parameter. From the previous simulation, couplers with $30dB$ crosstalk are chosen to construct the resonator. Other parameters are listed in Table 5.7 and Table 5.8. From the result, we can conclude that the system shows some tolerance of splicing rotation misalignment.

(5) Demodulation error with different input state of polarization

Figure 5.15 and Fig. 5.16 show the demodulation error as a function of phase difference with input state of polarization (SOP) as the parameter. The parameters are listed in Table 5.9 and Table 5.10. The SOP of the CW side is assumed to be linear with its polarization axis the same as the $x-$ axis. From the results it can be concluded that the circular SOP causes the largest error when the phase difference of the two ESOPs are π. This is because it almost equally excites two ESOPs. Under the same condition, the 0.1^o linearly polarized light has the best performance as its polarization axis is the closest to one of the ESOPs. This also demonstrates the advantage of the twice 90^o rotation splicing configuration that by controlling the phase difference of the two ESOPs, we are capable to excite only one of them by injecting linearly polarized light.

(6) Demodulation error with different finesse

Figure 5.17 and Fig. 5.18 show the demodulation error as a function of phase difference with R-FOG finesse as the parameter. The parameters are listed in Table 5.11 and Table 5.12. From the simulation results, it can be concluded that the higher the finesse, the higher the system sensitivity. Besides, with moderate finesse and careful alignment of the splicing point, this system shows some tolerance to the ESOP drift when they are close to π.

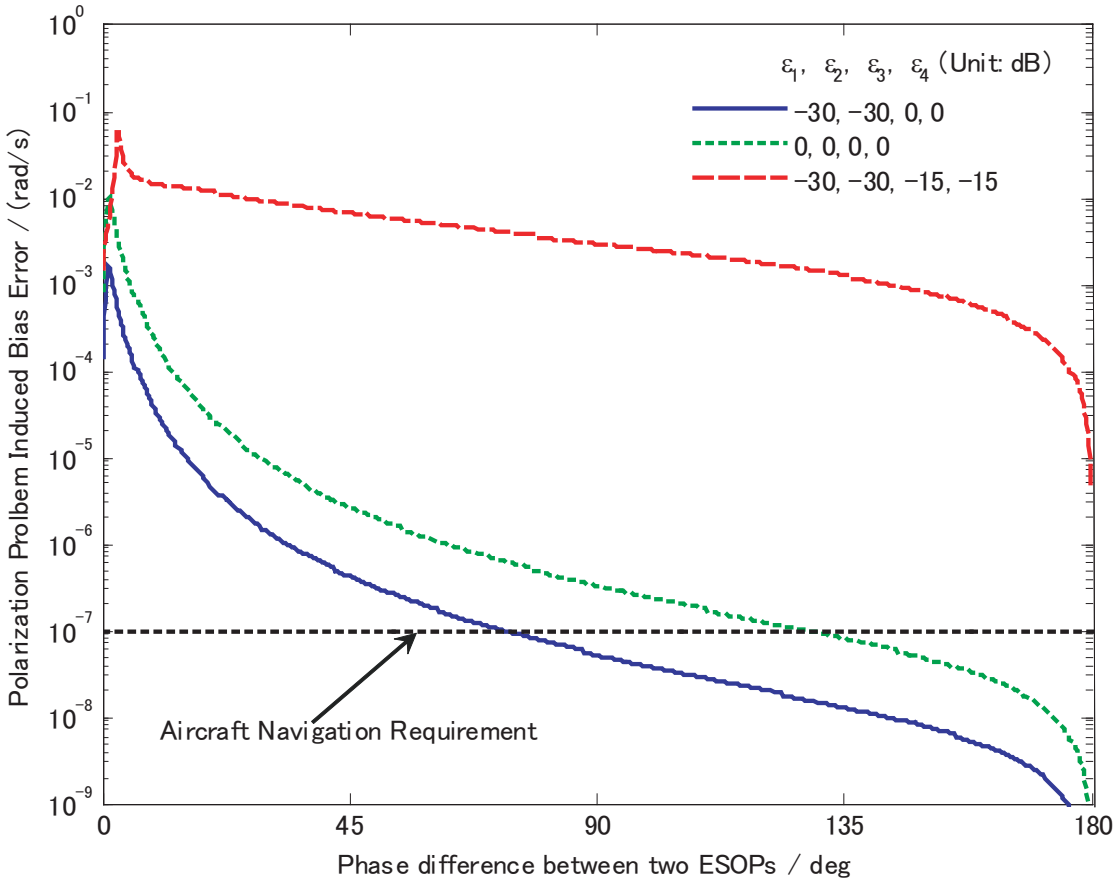

FIG. 5.7: Demodulation error with different polarizer extinction ratio: $\theta_2 : 90.2^o$.

TABLE 5.1: Parameter List: Demodulation error (polarizer extinction ratio as parameter)

Para.	Value	Para.	Value	Para.	Value	Para.	Value
$\gamma_{x,1}$	0.1	$\gamma_{y,1}$	0.1	$\kappa_{x,1}$	0.99	$\kappa_{y,1}$	0.99
$\gamma_{x,2}$	0.1	$\gamma_{y,2}$	0.1	$\kappa_{x,2}$	0.99	$\kappa_{y,2}$	0.99
L_1	2.5	L_2	2.5	L_3	2.5	L_4	2.5
L_B	$3mm$	α_x	$0.3dB/km$	α_y	$0.4dB/km$	n	1.46
CT_1	$30dB$	CT_2	$30dB$	θ_1	89.9^o	f_{rp}	$100kHz$
λ	$1.55\mu m$	$E_{i,ccw}$	$5^o, linear$	$E_{i,cw}$	$0^o, linear$		

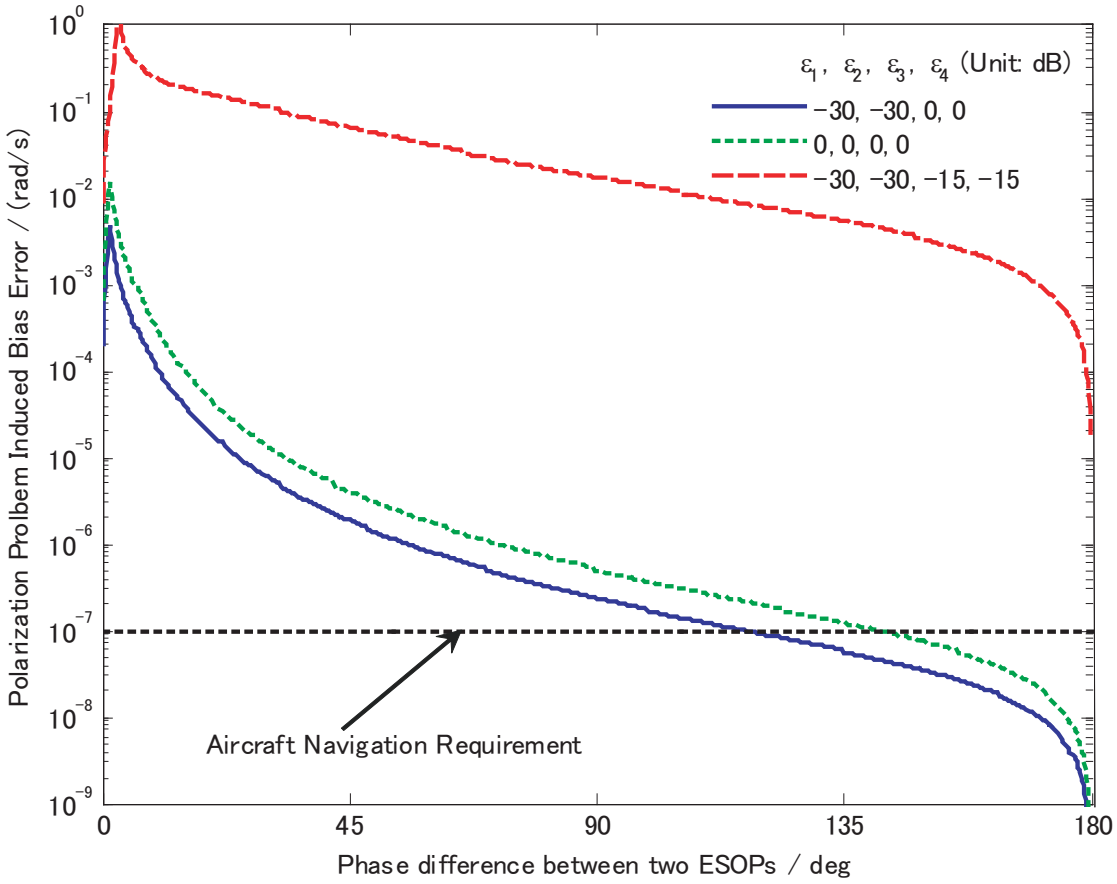

FIG. 5.8: Demodulation error with different polarizer extinction ratio: $\theta_2 : 95^o$.

TABLE 5.2: Parameter List: Demodulation error (polarizer extinction ratio as parameter)

Para.	Value	Para.	Value	Para.	Value	Para.	Value
$\gamma_{x,1}$	0.1	$\gamma_{y,1}$	0.1	$\kappa_{x,1}$	0.99	$\kappa_{y,1}$	0.99
$\gamma_{x,2}$	0.1	$\gamma_{y,2}$	0.1	$\kappa_{x,2}$	0.99	$\kappa_{y,2}$	0.99
L_1	2.5	L_2	2.5	L_3	2.5	L_4	2.5
L_B	$3mm$	α_x	$0.3dB/km$	α_y	$0.4dB/km$	n	1.46
CT_1	$30dB$	CT_2	$30dB$	θ_1	89.9^o	f_{rp}	$100kHz$
λ	$1.55\mu m$	$E_{i,ccw}$	$5^o, linear$	$E_{i,cw}$	$0^o, linear$		

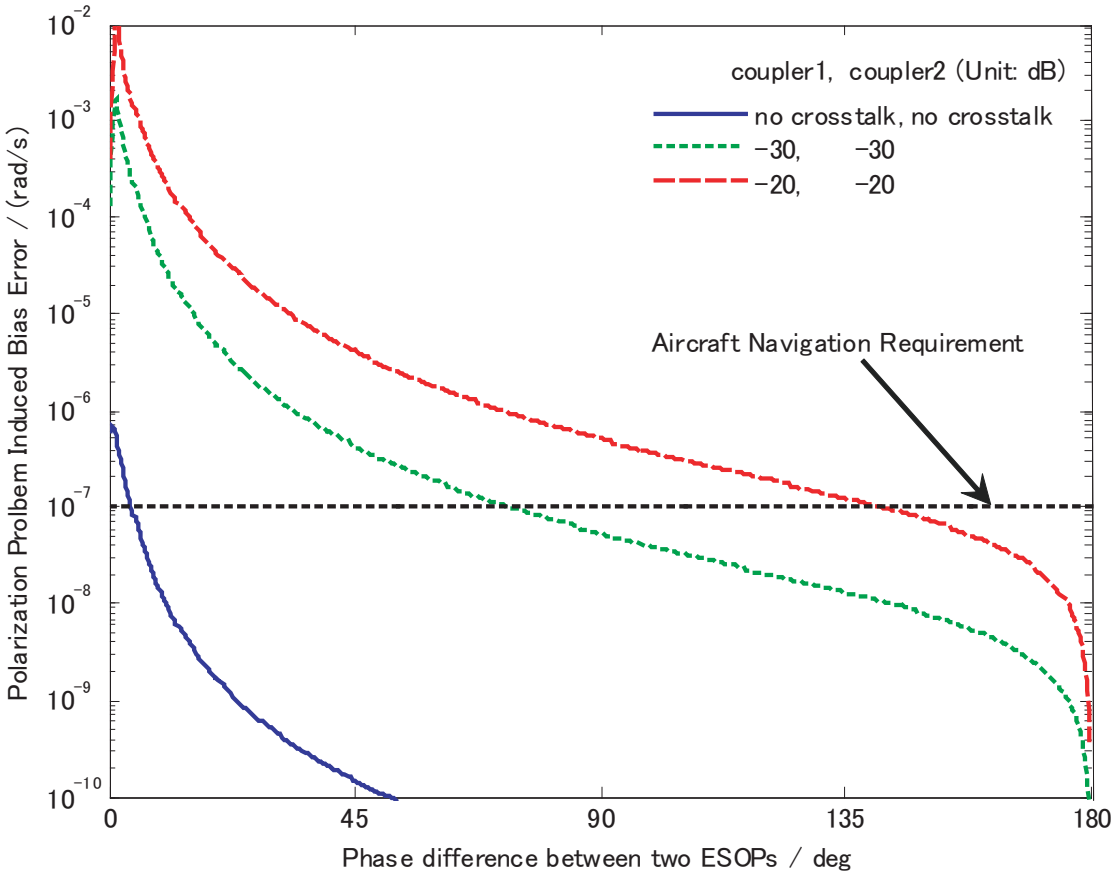

FIG. 5.9: Demodulation error with different crosstalk in the coupler: $E_{i,ccw}$: $1^o, linear$.

TABLE 5.3: Parameter List: Demodulation error (coupler crosstalk as parameter)

Para.	Value	Para.	Value	Para.	Value	Para.	Value
$\gamma_{x,1}$	0.1	$\gamma_{y,1}$	0.1	$\kappa_{x,1}$	0.99	$\kappa_{y,1}$	0.99
$\gamma_{x,2}$	0.1	$\gamma_{y,2}$	0.1	$\kappa_{x,2}$	0.99	$\kappa_{y,2}$	0.99
L_1	2.5	L_2	2.5	L_3	2.5	L_4	2.5
L_B	$3mm$	α_x	$0.3dB/km$	α_y	$0.4dB/km$	n	1.46
ϵ_1	$30dB$	ϵ_2	$30dB$	θ_1	89.9^o	θ_2	90.2^o
λ	$1.55\mu m$	$E_{i,cw}$	$0^o, linear$	f_{rp}	$100kHz$		

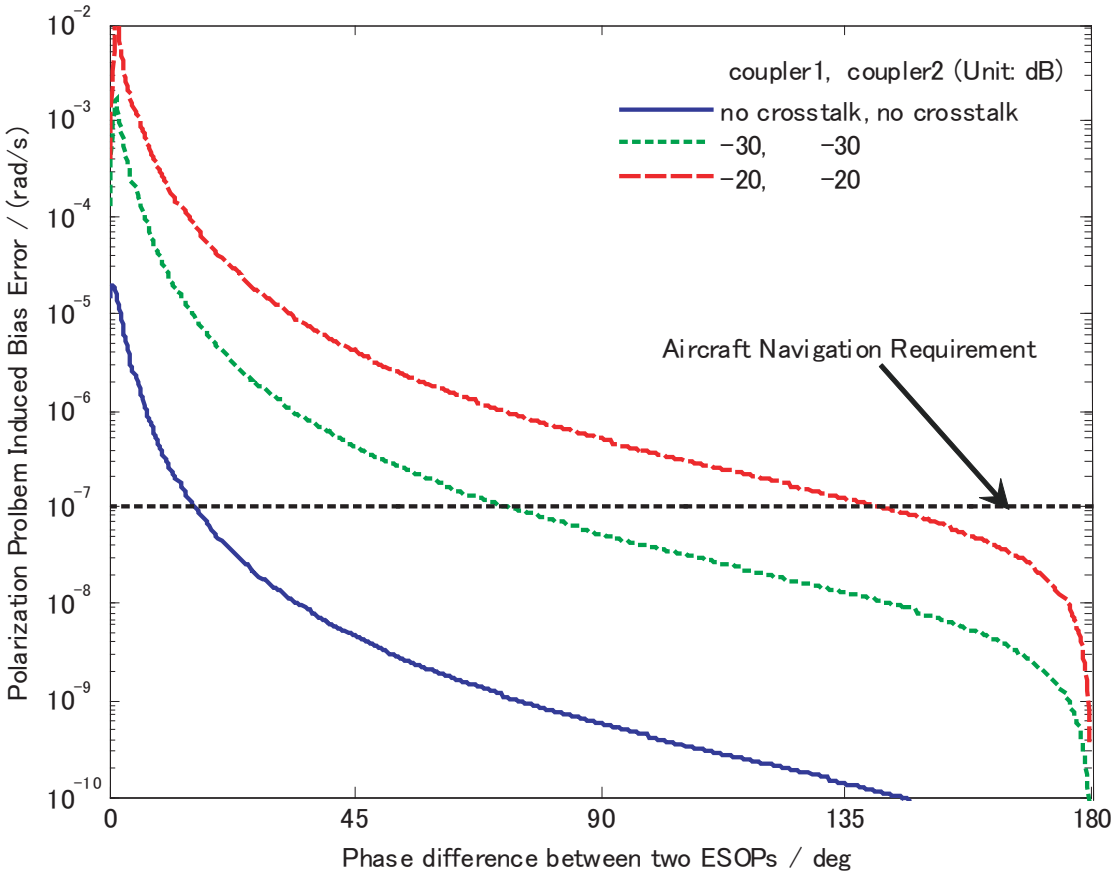

FIG. 5.10: Demodulation error with different crosstalk in the coupler: $E_{i,ccw}$: $5^o, linear$.

TABLE 5.4: Parameter List: Demodulation error (coupler crosstalk as parameter)

Para.	Value	Para.	Value	Para.	Value	Para.	Value
$\gamma_{x,1}$	0.1	$\gamma_{y,1}$	0.1	$\kappa_{x,1}$	0.99	$\kappa_{y,1}$	0.99
$\gamma_{x,2}$	0.1	$\gamma_{y,2}$	0.1	$\kappa_{x,2}$	0.99	$\kappa_{y,2}$	0.99
L_1	2.5	L_2	2.5	L_3	2.5	L_4	2.5
L_B	$3mm$	α_x	$0.3dB/km$	α_y	$0.4dB/km$	n	1.46
ϵ_1	$30dB$	ϵ_2	$30dB$	θ_1	89.9^o	θ_2	90.2^o
λ	$1.55\mu m$	$E_{i,cw}$	$0^o, linear$	f_{rp}	$100kHz$		

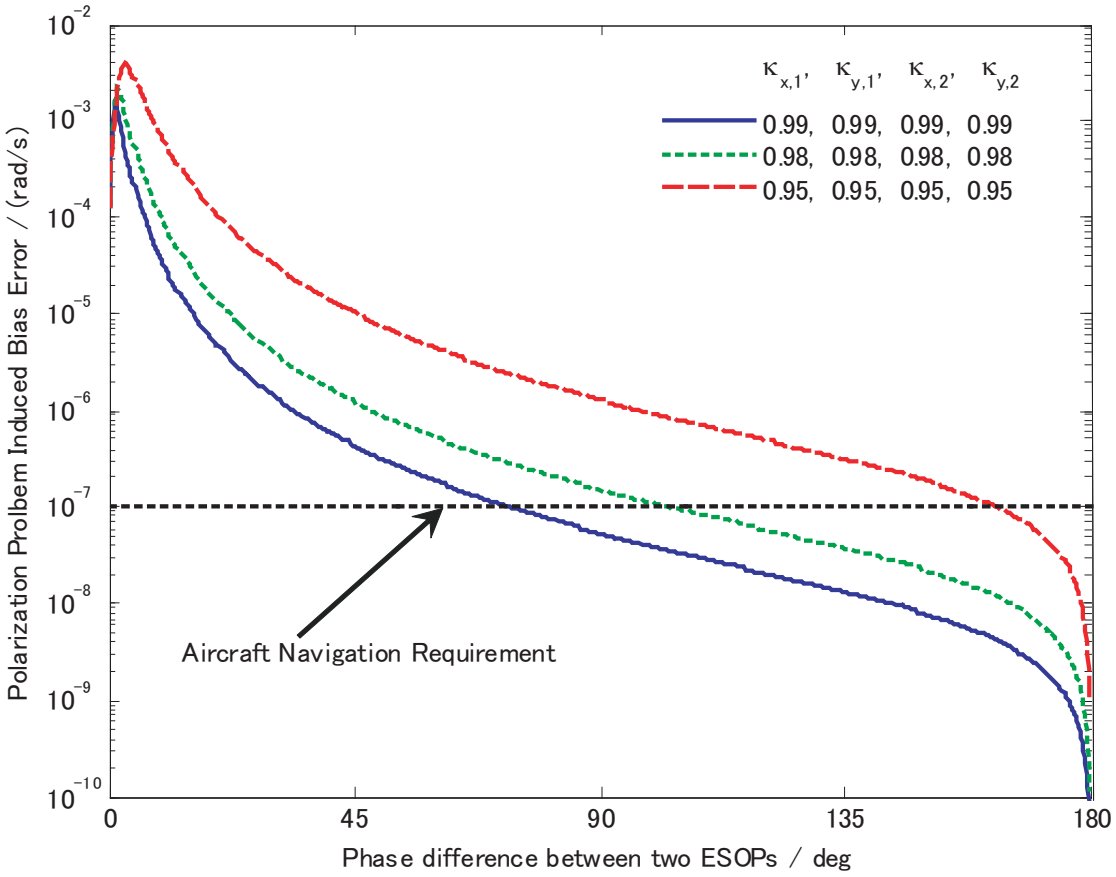

FIG. 5.11: Demodulation error with different coupling constant in the coupler.

TABLE 5.5: Parameter List: Demodulation error (coupler coupling constant as parameter)

Para.	Value	Para.	Value	Para.	Value	Para.	Value
$\gamma_{x,1}$	0.1	$\gamma_{y,1}$	0.1	$\gamma_{x,1}$	0.1	$\gamma_{y,1}$	0.1
L_1	2.5	L_2	2.5	L_3	2.5	L_4	2.5
L_B	$3mm$	α_x	$0.3dB/km$	α_y	$0.4dB/km$	n	1.46
ϵ_1	$30dB$	ϵ_2	$30dB$	θ_1	89.9^o	θ_2	90.2^o
λ	$1.55\mu m$	E_i	$1^o, linear$	$E_{i,cw}$	$0^o, linear$	f_{rp}	$100kHz$
CT_1	$30dB$	CT_2	$30dB$				

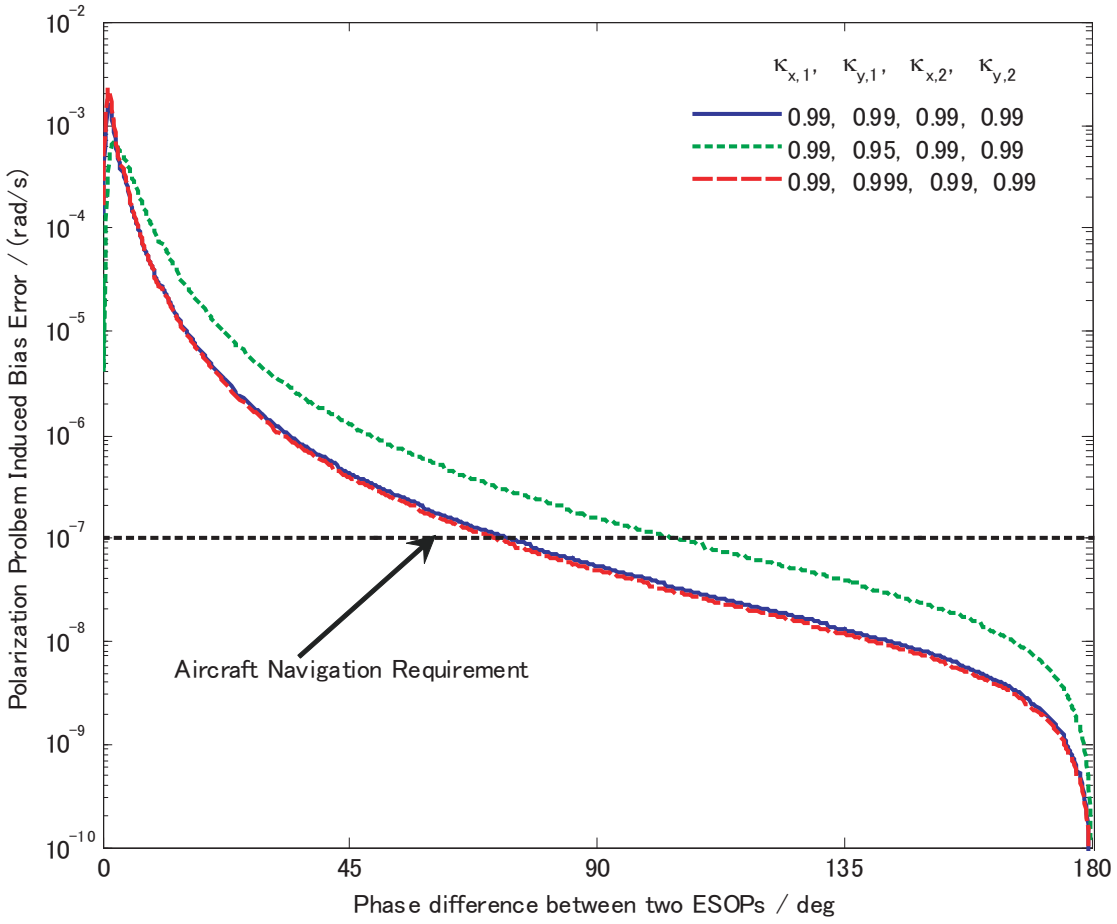

FIG. 5.12: Demodulation error with different coupling constant in the coupler.

TABLE 5.6: Parameter List: Demodulation error (coupler coupling constant as parameter)

Para.	Value	Para.	Value	Para.	Value	Para.	Value
$\gamma_{x,1}$	0.1	$\gamma_{y,1}$	0.1	$\gamma_{x,1}$	0.1	$\gamma_{y,1}$	0.1
L_1	2.5	L_2	2.5	L_3	2.5	L_4	2.5
L_B	$3mm$	α_x	$0.3dB/km$	α_y	$0.4dB/km$	n	1.46
ϵ_1	$30dB$	ϵ_2	$30dB$	θ_1	89.9^o	θ_2	90.2^o
λ	$1.55\mu m$	E_i	$1^o, linear$	$E_{i,cw}$	$0^o, linear$	f_{rp}	$100kHz$
CT_1	$30dB$	CT_2	$30dB$				

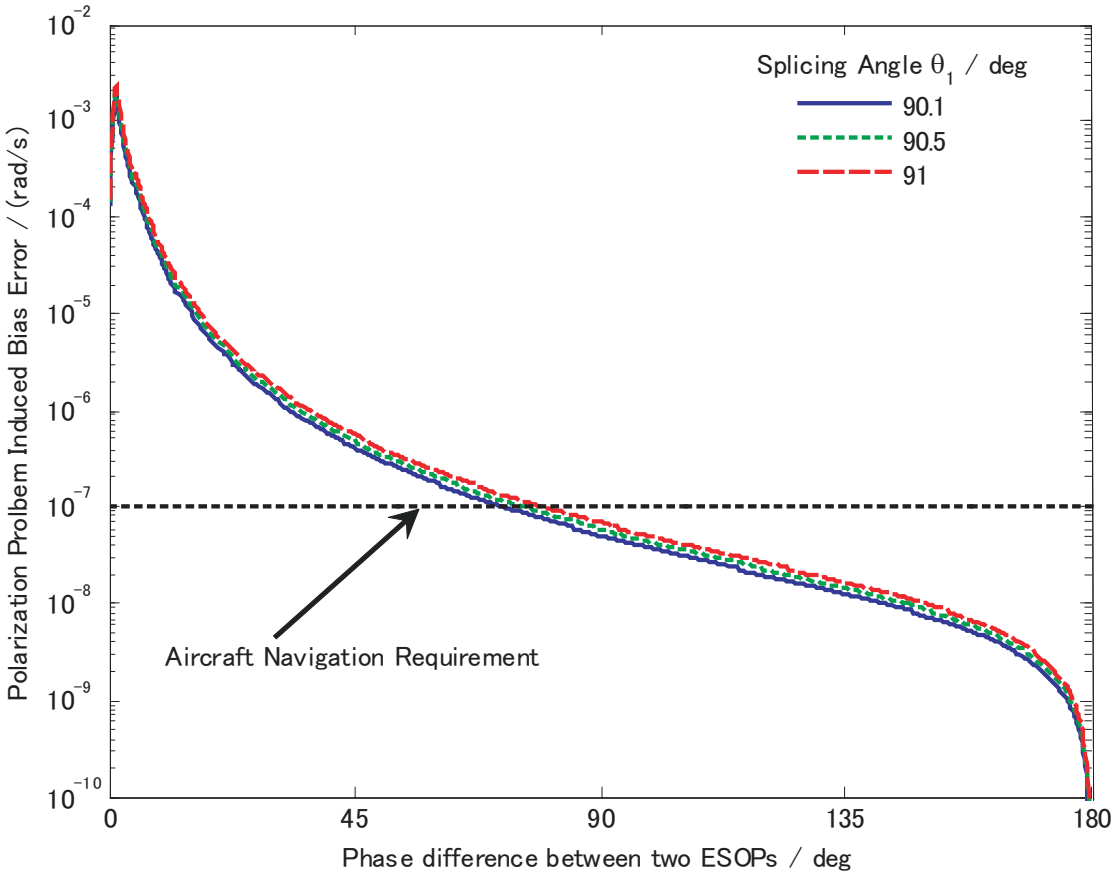

FIG. 5.13: Demodulation error with different splicing rotation angle: $\theta_2 : 90^o$.

TABLE 5.7: Parameter List: Demodulation error (rotation splicing angle as parameter)

Para.	Value	Para.	Value	Para.	Value	Para.	Value
$\gamma_{x,1}$	0.1	$\gamma_{y,1}$	0.1	$\kappa_{x,1}$	0.99	$\kappa_{y,1}$	0.99
$\gamma_{x,2}$	0.1	$\gamma_{y,2}$	0.1	$\kappa_{x,2}$	0.99	$\kappa_{y,2}$	0.99
L_1	2.5	L_2	2.5	L_3	2.5	L_4	2.5
L_B	$3mm$	α_x	$0.3dB/km$	α_y	$0.4dB/km$	n	1.46
ϵ_1	$30dB$	ϵ_2	$30dB$	CT_1	$30dB$	CT_2	$30dB$
λ	$1.55\mu m$	$E_{i,ccw}$	$1^o, linear$	$E_{i,cw}$	$0^o, linear$	f_{rp}	$100kHz$

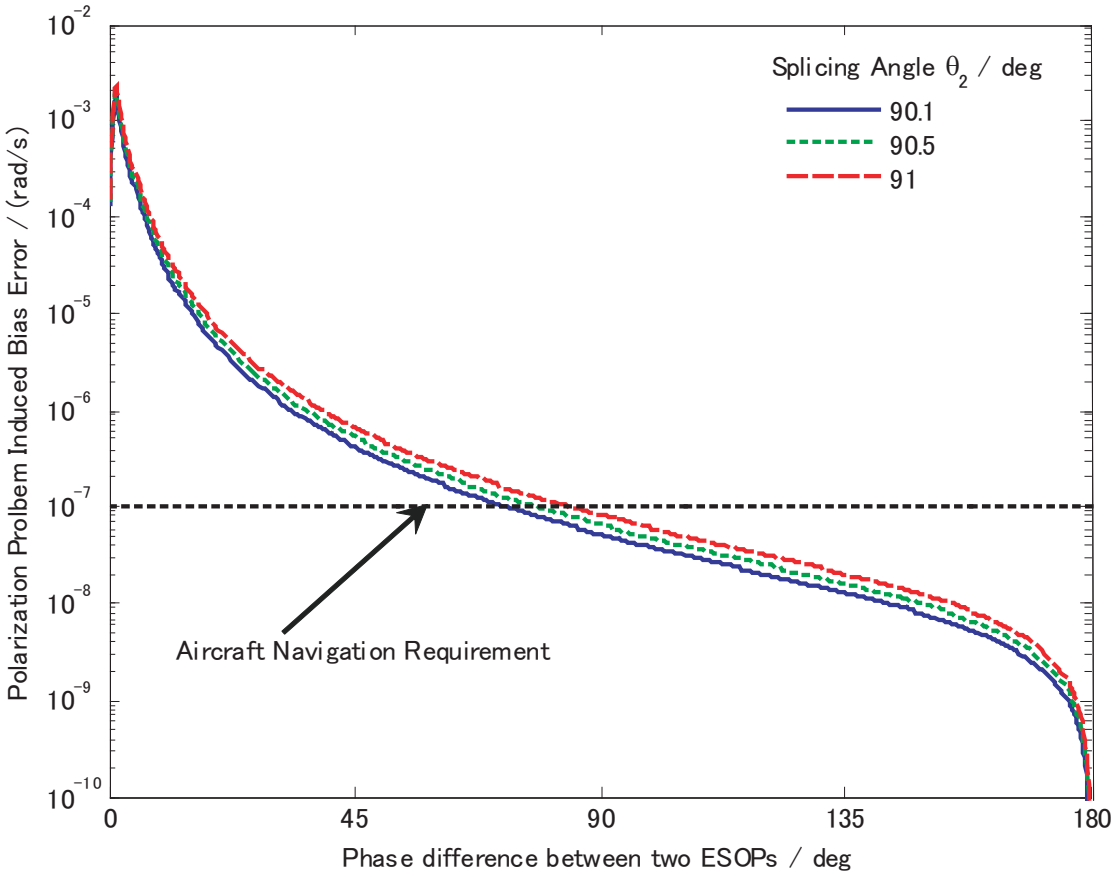

FIG. 5.14: Demodulation error with different splicing rotation angle: $\theta_1 : 90^o$.

TABLE 5.8: Parameter List: Demodulation error (rotation splicing angle as parameter)

Para.	Value	Para.	Value	Para.	Value	Para.	Value
$\gamma_{x,1}$	0.1	$\gamma_{y,1}$	0.1	$\kappa_{x,1}$	0.99	$\kappa_{y,1}$	0.99
$\gamma_{x,2}$	0.1	$\gamma_{y,2}$	0.1	$\kappa_{x,2}$	0.99	$\kappa_{y,2}$	0.99
L_1	2.5	L_2	2.5	L_3	2.5	L_4	2.5
L_B	$3mm$	α_x	$0.3dB/km$	α_y	$0.4dB/km$	n	1.46
ϵ_1	$30dB$	ϵ_2	$30dB$	CT_1	$30dB$	CT_2	$30dB$
λ	$1.55\mu m$	$E_{i,ccw}$	$1^o, linear$	$E_{i,cw}$	$0^o, linear$	f_{rp}	$100kHz$

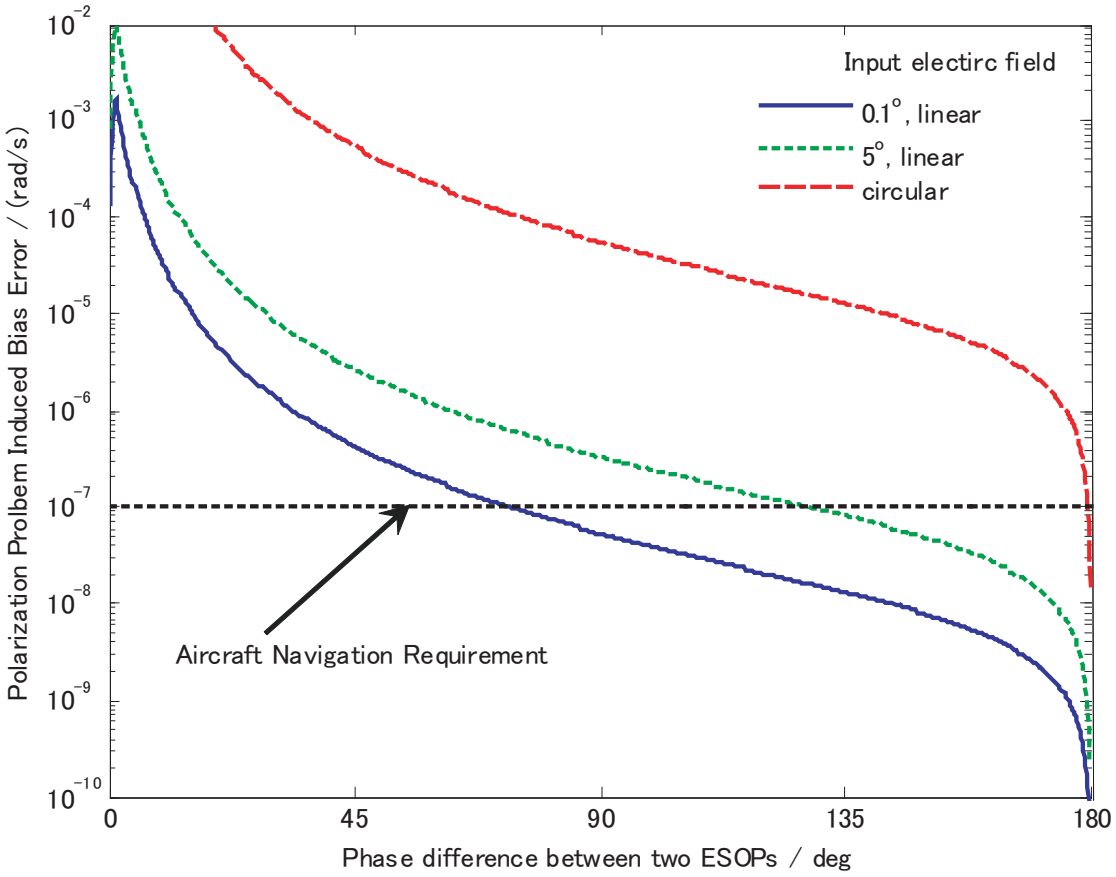

FIG. 5.15: Demodulation error with different input state of polarization: $\theta_2 : 90.2^o$.

TABLE 5.9: Parameter List: Demodulation error (input state of polarization as parameter)

Para.	Value	Para.	Value	Para.	Value	Para.	Value
$\gamma_{x,1}$	0.1	$\gamma_{y,1}$	0.1	$\kappa_{x,1}$	0.99	$\kappa_{y,1}$	0.99
$\gamma_{x,2}$	0.1	$\gamma_{y,2}$	0.1	$\kappa_{x,2}$	0.99	$\kappa_{y,2}$	0.99
L_1	2.5	L_2	2.5	L_3	2.5	L_4	2.5
L_B	$3mm$	α_x	$0.3dB/km$	α_y	$0.4dB/km$	n	1.46
ϵ_1	$30dB$	ϵ_2	$30dB$	θ_1	89.9^o	λ	$1.55\mu m$
CT_1	$30dB$	CT_2	$30dB$	$E_{i,cw}$	$0^o, linear$	f_{rp}	$100kHz$

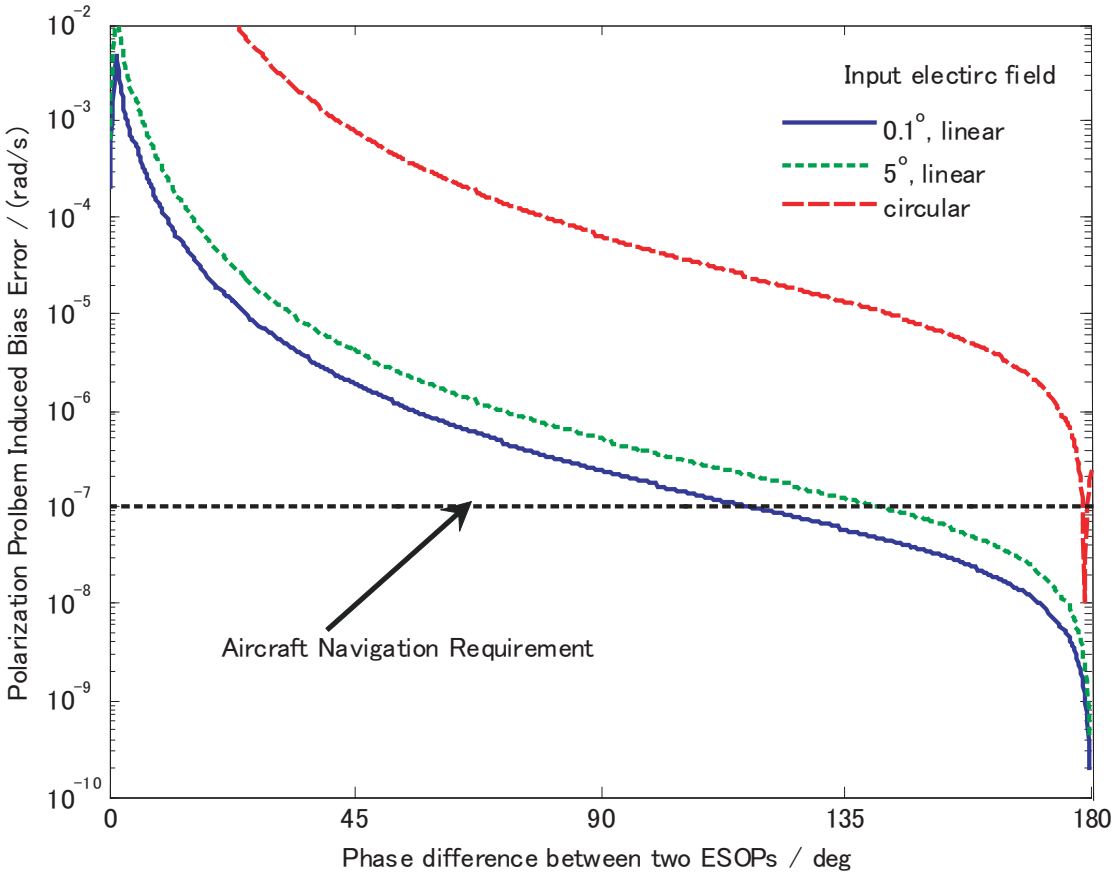

FIG. 5.16: Demodulation error with different input state of polarization: $\theta_2 : 95^o$.

TABLE 5.10: Parameter List: Demodulation error (input state of polarization as parameter)

Para.	Value	Para.	Value	Para.	Value	Para.	Value
$\gamma_{x,1}$	0.1	$\gamma_{y,1}$	0.1	$\kappa_{x,1}$	0.99	$\kappa_{y,1}$	0.99
$\gamma_{x,2}$	0.1	$\gamma_{y,2}$	0.1	$\kappa_{x,2}$	0.99	$\kappa_{y,2}$	0.99
L_1	2.5	L_2	2.5	L_3	2.5	L_4	2.5
L_B	$3mm$	α_x	$0.3dB/km$	α_y	$0.4dB/km$	n	1.46
ϵ_1	$30dB$	ϵ_2	$30dB$	θ_1	89.9^o	λ	$1.55\mu m$
CT_1	$30dB$	CT_2	$30dB$	$E_{i,cw}$	$0^o, linear$	f_{rp}	$100kHz$

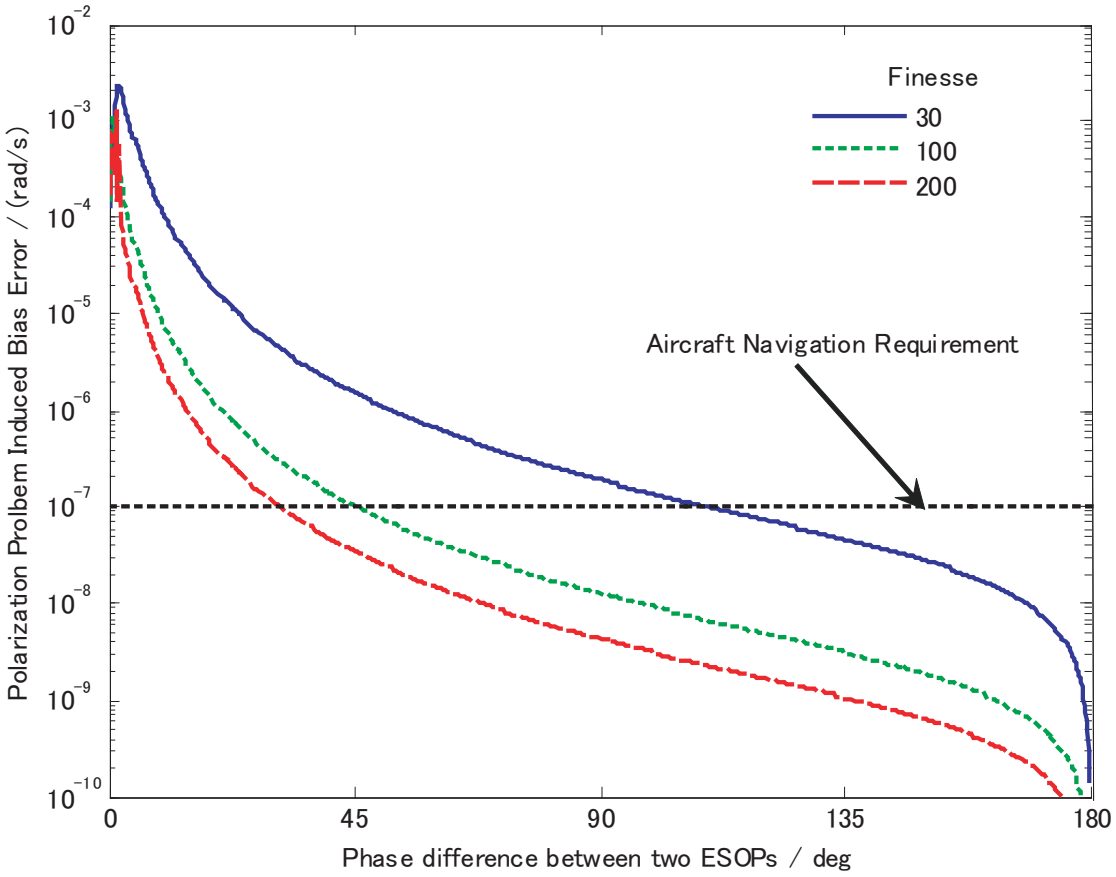

FIG. 5.17: Demodulation error with different finesse: $\theta_2 : 90.2^o$.

TABLE 5.11: Parameter List: Demodulation error (finesse as parameter)

Para.	Value	Para.	Value	Para.	Value	Para.	Value
$\kappa_{x,1}$	0.99	$\kappa_{y,1}$	0.99	$\kappa_{x,2}$	0.99	$\kappa_{y,2}$	0.99
L_1	2.5	L_2	2.5	L_3	2.5	L_4	2.5
L_B	$3mm$	α_x	$0.3dB/km$	α_y	$0.4dB/km$	n	1.46
ϵ_1	$30dB$	ϵ_2	$30dB$	θ_1	89.9^o	λ	$1.55\mu m$
$CT_{1,2}$	$30dB$	$E_{i,ccw}$	$1^o, linear$	$E_{i,cw}$	$0^o, linear$	f_{rp}	$100kHz$

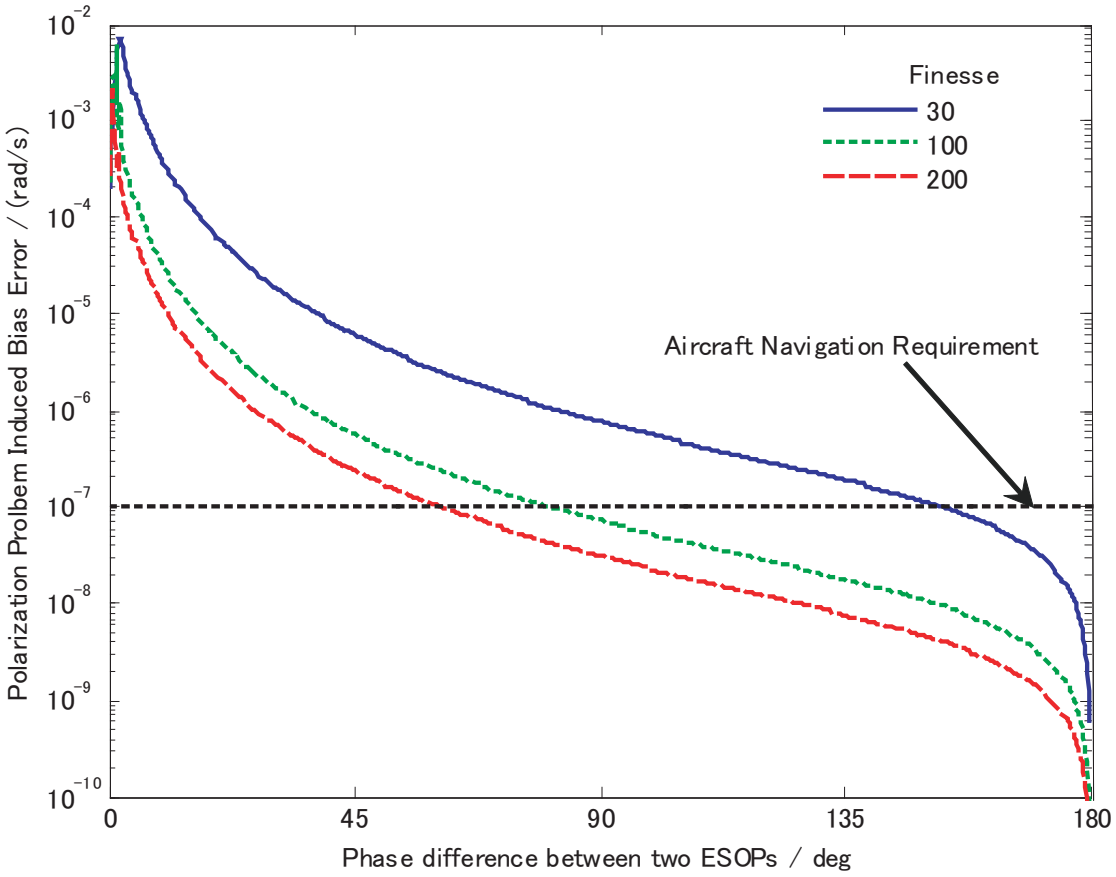

FIG. 5.18: Demodulation error with different finesse: $\theta_2 : 95^o$.

TABLE 5.12: Parameter List: Demodulation error (finesse as parameter)

Para.	Value	Para.	Value	Para.	Value	Para.	Value
$\kappa_{x,1}$	0.99	$\kappa_{y,1}$	0.99	$\kappa_{x,2}$	0.99	$\kappa_{y,2}$	0.99
L_1	2.5	L_2	2.5	L_3	2.5	L_4	2.5
L_B	$3mm$	α_x	$0.3dB/km$	α_y	$0.4dB/km$	n	1.46
ϵ_1	$30dB$	ϵ_2	$30dB$	θ_1	89.9^o	λ	$1.55\mu m$
$CT_{1,2}$	$30dB$	$E_{i,ccw}$	$1^o, linear$	$E_{i,cw}$	$0^o, linear$	f_{rp}	$100kHz$

5.3.2 Discussion

In the previous sections, we have numerically analyzed the demodulation error in different system parameters. It should be noted that in the ideal case of twice 90^o rotation splicing and no coupler crosstalk, the eigenvector is:

$$v1 = [1, 0]^T, v2 = [0, 1]^T \tag{5.21}$$

which is extremely useful in R-FOG. Under this situation, the two ESOPs are the same as that of the two polarization axes. What's more we can write out the phase difference:

$$\Delta\phi = \Delta\beta\Delta L \tag{5.22}$$

where $\Delta L = (L_1 + L4) - (L_2 + L_3)$. Two merits are quite obvious: (1) if we set the two ESOPs π away from each other with proper control, the aircraft navigation requirement can be reached; (2) since ΔL is several times smaller than the total length L, the phase drift caused by a similar temperature variation can be largely reduced.

In unideal conditions, when the ESOPs are π away from each other, the bias error induced by polarization drift problem is expected to be low. This can be explained by Fig. 5.19. The solid lines in black show the ESOPs under the ideal condition. The solid blue line and the dashed red line represent the two ESOPs when the fiber at the splicing point is misaligned. The misalignment angles of $\theta_{1,2}$ are 80^o and 91^o, respectively. The ESOPs change from circular to elliptic to linear and to circular again when the phase difference vary from zero to $\pi/4$ to π to 2π. It should be noted that by settling the phase difference to π, the ESOPs are linearly polarized. So we can selectively excite only one of them, which reduces the bias error by a large amount.

5.4 Conclusion

In this section, we first build a novel mathematical that includes the crosstalk in the coupler as one of the parameters in a twice 90^o rotation spliced resonator. By numerical simulation, we find that this is a more general and realistic model than the previously reported one. Besides, by removing the two polarizers at the exit, the system performance is greatly increased. With this scheme as a treatment of polarization problem, high grade R-FOG can be constructed in condition that the two ESOPs are π phase away from each other.

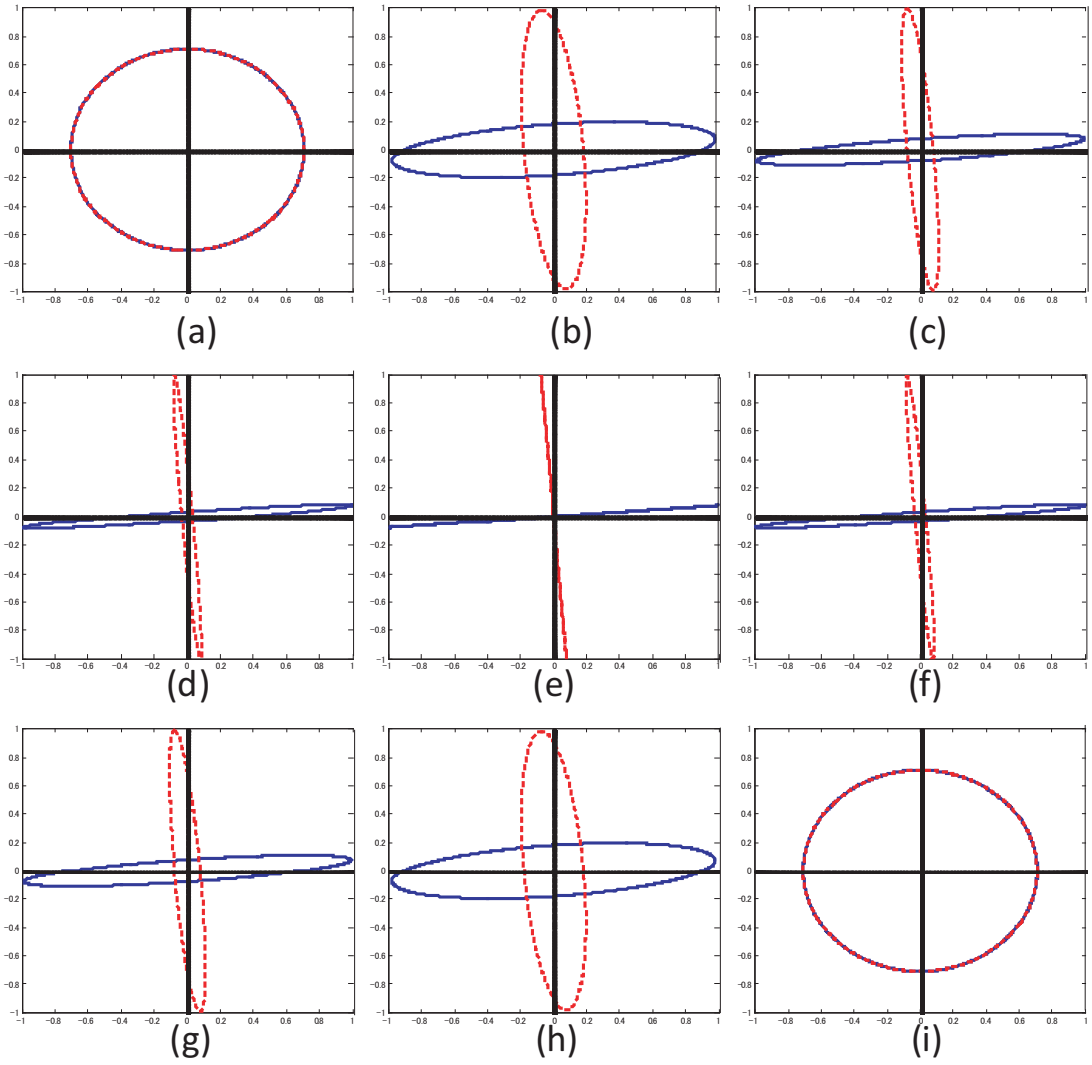

FIG. 5.19: ESOPs as a function of phase difference: (a) 0; (b) $pi/4$; (c) $pi/2$; (d) $3\pi/4$; (e) pi; (f) $5\pi/4$; (g) $3\pi/2$; (h) $5\pi/4$; (i) 2π.

Chapter 6

Conclusion

6.1 Conclusion

In this thesis, we have analyzed the noise factors and their anti-measurement in the R-FOG both theoretically and experimentally.

At first, we have realized that the traditional PMF itself in R-FOG remains as the source of noise that can not be further reduced. To overcome this difficulty, we propose to construct the resonator with the novel PBF, which is reported to be low in backscattering coefficient, Kerr effect, Shupe effect, and temperature coefficient. The PBF resonator based on bulk optics is built and its resonant characteristics are tested. It is also found that the PMF is less sensitive to temperature changes, which is positive to the rotation detection in R-FOG.

Next, we developed a digital controller that is capable of tracking laser diode central frequency drift, compensating for imperfect 2π voltage of phase modulator, and reading out the frequency difference between CW and CCW side. To separate the algorithm problem from the fiber optical system noise, we compile the algorithms in a separate PMF based R-FOG system. It shows much higher flexibility as compared with the traditional analogue systems. Under the control of this digital processor, we have successfully detected a quasi-rotation signal with a sensitivity of $0.8^o/s$.

Finally, the polarization problem is analyzed based on a two 90^o splicing scheme. It is for the first time that both the crosstalk in the coupler and the splicing rotation angle error are incorporated in one model. Simulation results show that the crosstalk can not be ignored in a R-FOG. Besides, with this scheme, we can achieve the aircraft navigation requirement by adjusting the resonator parameters.

6.2 Future Work

First of all, the rotation experiment based on the PBF R-FOG should be carried out. This requires a resonator with more stable performance and higher finesse. And this can be solved if PBF based optical passive components are produced. Otherwise, free space alignment system should be reconsidered.

Secondly, the analogue loop which tracks the fast drift in the laser diode in our digital controller should be removed. This requires a faster digital controller with higher processing power. One possible solution might be the application of FPGA which is commonly used in feedback control loops.

Thirdly, anti-measurement for the Kerr effect should be proposed and tested in the digital controller. This can be realized by incorporating another feedback loop to balance the input lightwave intensities of the CW and CCW side.

By combining the above aspects in one system, we are on the prospect of building a R-FOG with medium to high grade.

Bibliography

[1] K. Hotate, "Fiber-optic gyros," in *Optical Fiber Sensors* (J. Dakin and B. Culshaw, eds.), vol. 4, ch. 11, Artech House, 1997.

[2] H. Lefevre, *The Fiber-Optic Gyroscope*. Artech House, 1993.

[3] K. Hotate and G. Hayashi, "Resonator fiber optic gyro using digital serrodyne modulation method to reduce the noise induced by the backscattering and closed-loop operation using digital signal processing," in *Proc. 13th International Conference on Optical Fiber Sensors*, Tu4-1, 1999.

[4] K. Hotate and M. Harumoto, "Resonator fiber optic gyro using digital serrodyne modulation," *J. Lightwave Technol.*, vol. 15, no. 3, pp. 466–473, 1997.

[5] K. Iwatsuki, K. Hotate, and M. Higashiguchi, "Effect of rayleigh backscattering in an optical passive ring-resonator gyro," *Appl. Opt.*, vol. 23, no. 21, pp. 3916–3924, 1984.

[6] K. Hotate, K. Takiguchi, and A. Hirose, "Adjustment-free method to eliminate the noise induced by the backscattering in an optical passive ring-resonator gyro," *IEEE Photon. Technol. Lett.*, vol. 2, no. 1, pp. 75 – 77, 1990.

[7] K. Iwatsuki, K. Hotate, and M. Higashiguchi, "Eigenstate of polarization in a fiber ring resonator and its effect in an optical passive ring- resonator gyro," *Appl. Opt.*, vol. 25, no. 15, pp. 2606–2612, 1986.

[8] K. Takiguchi and K. Hotate, "Bias of an optical passive ring-resonator gyro caused by the misalignment of the polarization axis in the polarization-maintaining fiber resonator," *J. Lightwave Technol.*, vol. 10, no. 4, pp. 514–522, 1992.

[9] G. A. Sanders, R. B. Smith, and G. F. Rouse, "Novel polarization-rotating fiber resonator for rotation applications," in *Proc. SPIE*, vol. 1169, pp. 373–381, 1989.

[10] K. Takiguchi and K. Hotate, "Method to reduce the optical kerr-effect-induced bias in an optical passive ring-resonator gyroscope," *IEEE Photon. Technol. Lett.*, vol. 4, no. 2, pp. 203 – 206, 1992.

[11] M. Inai and K. Hotate, "Proposal and experimental result of method to reduce the noise induced by optical kerr effect for resonator fiber optic gyro using digital serrodyne modulation," in *IEICE*, 2004.

[12] D. M. Shupe, "Fiber resonator gyroscope: sensitivity and thermal nonreciprocity," *Appl. Opt.*, vol. 20, no. 21, pp. 286–289, 1981.

[13] J. C. Knight and P. S. J. Russell, "New ways to guide light," *Science*, vol. 296, pp. 276–277, 2002.

[14] P. Russell, "Photonic crystal fibers," *Science,*, vol. 299, pp. 358–362, 2003.

[15] A. Yariv and P. Yeh, *Photonics*. Oxford University Press, 6 ed., 2007.

[16] H. K. Kim, M. J. F. Digonnet, and G. S. Kino, "Air-core photonic-bandgap fiber-optic gyroscope," *J. Lightwave Technol.*, vol. 24, no. 8, pp. 3169–3174, 2006.

[17] V. Dangui, H. K. Kim, M. J. F. Dinonnet, and G. S. Kino, "Theoretical and experimental study of the fundamental mode propagation phase temperature sensitivity in air-core photonic-bandgap fibers," in *Proc. Optical Fiber Communication Conference*, OTu14, 2005.

[18] G. D. Ouzounov, F. R. Ahmad, D. Muller, and et al., "Generation megawatt optical solitons in hollow-core photonic band-gap fibers," *Science*, vol. 301, no. 5640, pp. 1702–1704, 2003.

[19] L. K. Strandjord and G. A. Sanders, "Effects of imperfect serrodyne phase modulation in resonator fiber optic gyroscopes," in *Proc. SPIE*, vol. 2292 of *2292*, pp. 272–282, 1994.

[20] Z. K. Ionaidis, R. Kadjwar, and I. P. Giles, "Anisotropic polarization maintaining optical fiber ring resonators," *J. Lightwave Technol.*, vol. 14, no. 3, pp. 377–384, 1996.

[21] H. Kazuo and N. Hitoshi, "Analysis of a method to reduce polarization fluctuation-induced bias drift in resonator fiber-optic gyros," in *IEICE technical report. Microwaves*, vol. 101, pp. 13–18, 2001.

[22] Z. K. Ioannidis, R. Kasiwar, and I. P. Giles, "Polarization mode coupling in highly birefringent optical-fiber ring resonators," *Opt. Lett.*, vol. 14, no. 10, pp. 520–522, 1989.

Publication List

[1] X.Wang, Z. He, and K. Hotate, "Rotation Experiment of Ring Resonator Fiber Optic Gyroscope with a Digital Controller," in *IEICE Conference on Optical Fiber Technology*, OFT2008-29, 2008.

[2] X. Wang, Z. He, S. Kawanishi, and K. Hotate, "Experimental Characterization of Ring Resonator Using Photonic Bandgap Fiber," in *IEICE General Conference of the Communication Society*, B-13-32, 2008.